




EX LIBRIS
UNIVERSITATIS
ALBERTENSIS

The Bruce Peel
Special Collections
Library



Digitized by the Internet Archive
in 2025 with funding from
University of Alberta Library

<https://archive.org/details/0162014233520>

University of Alberta

Library Release Form

Name of Author: Xiaowei Luo

Title of Thesis: Micro-Seismicities in Cold Heavy Oil Production and
Dispersion Phenomenon in Porous Media

Degree: Master of Science

Year this Degree Granted: 2001

Permission is hereby granted to the University of Alberta Library to reproduce single copies of this thesis and to lend or sell such copies for private, scholarly or scientific research purposes only.

The author reserves all other publication and other rights in association with the copyright in the thesis, and except as herein before provided, neither the thesis nor any substantial portion thereof may be printed or otherwise reproduced in any material form whatever without the author's prior written permission.

University of Alberta

**Micro-Seismicities in Cold Heavy Oil Production
and Dispersion Phenomenon in Porous Media**

by

Xiaowei Luo



A thesis submitted to the Faculty of Graduate Studies and Research in partial
fulfillment of the requirements for the degree of Master of Science
in
Geophysics

Department of Physics

Edmonton, Alberta

Fall 2001

University of Alberta

Faculty of Graduate Studies and Research

The undersigned certify that they have read, and recommend to the Faculty of Graduate Studies and Research for acceptance, a thesis entitled **Micro-Seismicities in Cold Heavy Oil Production and Dispersion Phenomenon in Porous Media** submitted by **Xiaowei Luo** in partial fulfillment of the requirements for the degree of Master of Science in Geophysics.

Abstract

This thesis consists of two parts. The first four chapters discuss the micro-seismicities in cold heavy oil production and the fifth chapter deals with the dispersion phenomenon of two-phase miscible flow in porous media.

In the first part, micro-seismic techniques were used in cold heavy oil production wells and these techniques proved to be able to monitor the sand production and the production tool operation. Micro-seismic events occur as a result of the sand production (a typical technology exploited in cold heavy oil production). The seismic data available was recorded by a three-component accelerometer. The dominant seismic events are classified, general techniques on determining the source parameters including the source location, focal mechanism, earthquake size, energy and the polarization direction are discussed, and then these parameters in the present case are estimated.

In the second part, the equations of the convection-diffusion theory and the dynamic equations of two-phase miscible flow are presented, and then the results of a set of dispersion experiments are discussed.

Acknowledgements

I would first like to thank my supervisor, Dr. Tim Spanos, for his supervision, assistance and support regarding the research contained in this thesis. Sincere thanks to the other professors in Geophysics including Dr. Doug Schmitt; Dr. Moritz Heimpel and Dr. Mauricio Sacchi who I have received help from. I would also like to thank fellow graduate students Jinsong Wang and Robert Zschuppe for their discussions and ideas pertaining to this thesis. I am also grateful to Kexian Au Yong for helping me with the dispersion experiments. I appreciate the help of Lynn Chandler who has worked hard and tirelessly for the benefit of the graduate students in our department. I would also give my thanks to the other students in Geophysics who have helped me with my thesis and the many other not so relevant topics.

Table of Contents

1. Introduction – Micro-Seismicities in Cold Heavy Oil Production	1
1.1. Cold Heavy Oil Production	1
1.1.1. Mechanisms of Cold Heavy Oil Production	1
1.1.2. Equipment	3
1.2. Pressure Pulsing Enhancement Technology	3
1.3. Micro-Seismic Technique	4
1.3.1. Source Mechanisms	4
1.3.2. Application of Micro-Seismic Techniques	5
1.3.3. Data Analysis Techniques	5
1.4. Micro-Seismic Techniques in Cold Heavy Oil Production	6
1.4.1. Purpose of Applying Micro-Seismic Techniques to Cold Heavy Oil Production	6
1.4.2. Micro-Seismic Activities in Cold Heavy Oil Production	7
2. Geology and Reservoir Setting	10
2.1. The Mannville Group of Sands	10
2.2. The Standard Heavy Oil Well on Cold Production	12
3. Instrumentation and Data Collection	14
3.1. Downhole Instrumentation	14
3.2. The Recording (ISS) Systems	16
3.3. Downhole Seismic Data	16
3.3.1. Average Continuous Monitoring Background Seismicity	17
3.3.2. Triggered Seismic Events	18
4. Data Analysis	28
4.1. Source Location	28
4.1.1. The Classic Least Squares Approach	29

4.1.2. Fedorov's Generalization of Least Squares Procedure	32
4.1.3. Relative Location Technique	34
4.1.4. Comparisons of Location Procedures	36
4.1.5. Location of Micro-Earthquakes in CHOP Wells	36
4.2. Focal Mechanisms of Micro-Earthquakes in CHOP Wells	36
4.2.1. Moment-Tensor Inversion	37
4.3. Micro-Earthquake Magnitude	41
4.3.1. Local Magnitude and Signal Duration Magnitude	42
4.4. Seismic Energy	43
4.5. Direction of Polarization	45
5. Two Phase Miscible Flow – the Dispersion Phenomenon in Porous Media	51
5.1. The Phenomenon of Dispersion	51
5.2. The Convection-Diffusion Theory	52
5.3. The Dynamical Equations of Two-Phase Flow	56
5.4. Experimental Results	58
6. Discussion	65
References	67

List of Figures

1-1 Configuration of a typical CHOP well	8
1-2 Conceptual schematic showing typical micro-seismic source mechanisms	9
2-1 A map showing the interpolated Sparky Sand thickness derived from well logs	13
3-1 Mounted accelerometers on 'Belly Spring' assembly	19
3-2 Average background noise created by the PC pump and the reservoir under normal condition	20
3-3 Triggered seismic events recorded on the average background noise	21
3-4 Average background noise indicating sand coming into the well bore	22
3-5 Tube wave generated by gas	23
3-6 Event generated by the pulse well due to failure of the hydraulic braking mechanisms on the pulse tool	24
3-7 Event generated by the pulse well	25
3-8 Sharp P-wave propagating in a homogeneous medium	26
3-9 Diffuse P-wave	27
4-1 Estimated micro-seismic source-receiver distance	48
4-2 Displacement of a typical sharp P-wave	49
4-3 Displacement of a typical diffuse P-wave	50
5-1 Spreading due to mechanical spreading (a), (b), and molecular diffusion (c)	60
5-2 An diagram showing the dispersion experiment setup	61
5-3 A picture showing the dispersion front at time 2.9s	62
5-4 A picture showing the dispersion front at time 13.4s	63
5-5 Longitudinal dispersion at four different cases	64

1. Introduction – Micro-Seismicities in Cold Heavy Oil Production

1.1. Cold Heavy Oil Production

Because of its unique physical and chemical properties, the economical production of heavy oil presents many obstacles. Heavy oil is very viscous and requires extensive upgrading, which makes production in large volumes difficult and expensive. Heavy oil reservoirs are also generally shallow and composed of unconsolidated (cohesionless) sand. In many instances, these physical properties and inherent conditions do not permit extraction of the oil from the reservoir using conventional oil technology. This has led to a focus on developing technologies suitable for the commercial exploitation of these heavy oil deposits.

One of the enhanced oil recovery methods that increase the heavy oil production rate is cold production. The term cold heavy oil production (CHOP) refers to the use of operating techniques and specialized pumping equipment to aggressively produce heavy oil reservoirs without applying heat. This encourages the associated production of large quantities of the unconsolidated reservoir sand, which in turn results in significantly higher oil production. CHOP is an enhanced oil recovery method that is applied during the primary production phase of oil extraction, and it has been called ‘Cold Primary Production’.

1.1.1. Mechanisms of Cold Heavy Oil Production

The basic mechanism of cold production is the sand production, which involves producing a part of the unconsolidated reservoir matrix together with the heavy crude oil. Heavy oil flows more efficiently when sand production occurs. Sand production relies on the unconsolidated nature of the reservoir — the absence of clays and cementation materials. The presence of clay or cementation materials will stabilize the sand grains and reduce sand movement, and high viscosity oil will increase the frictional drag between the sand grains and the oil. For high viscosity oil, if the sand is discouraged to move, the flow rate of oil will be low due to the high frictional drag

forces between the oil and the sand. But when the sand is allowed to move together with the oil, the flow rate will be increased because the fluid velocity increases with matrix movement, so the oil productivity is increased. This mechanism is hypothesized to result in a zone, the yielded zone, that is dilated and of enhanced permeability, or in the formation of 'wormholes' or channels. These 'wormholes' increase the permeability of the reservoir matrix, which facilitates the flow of the viscous and foamy oil into the wellbore. The foamy oil is the result of gas exsolution as bubbles as the reservoir pressure decreases with the withdrawal of reservoir fluids.

The primary reasons for enhanced production are (after Dusseault et al., 1998):

- "Fluid flow rate is increased if the sand matrix is allowed to move because the Darcy velocity relative to the solid matrix increases with matrix movement;"
- "As sand is produced from the reservoir, a zone of enhanced permeability is generated that propagates outward, allowing a greater fluid flux to the wellbore. Dilation or channels (wormholes) create a high permeability, radially expanding zone, which acts as a large radius well;"
- "A pressure drop leads to the generation of a 'foamy oil' zone, which helps drive the solids and fluids toward the wellbore."

The principal driving forces for the production of the sand and oil mixture may be summarized as below:

- a) Natural formation pressure
- b) Foamy oil drive: As the production process goes on, the formation pressure decreases, resulting in the exsolution of the gas originally dissolved in the oil. Under certain circumstances, this gas only exists in the form of gas bubbles; they do not form continuous gas phase. The oil in this condition is the so-called 'foamy oil'. Under decreasing pressure, these gas bubbles tend to expand, which drives the sand and oil toward the wellbore.
- c) Density difference between foamy zone and non-foamy zone: As the sand moves toward the wellbore, a density difference appears between the intact reservoir (non-foamy zone) and the area where the sand moves (foamy zone or yielded zone). To meet the law of conservation of mass on the boundary between these two regions, the sand in the higher density region will move

toward the lower density region, thus the boundary moves toward the intact region, and the foamy zone enlarges.

1.1.2. Equipment

The equipment usually used in cold production is a rotary drive, progressive cavity pumping system, commonly known as a screw pump. This kind of pump is used because of its ability to pump viscous fluid with high solid content. The progressive cavity pump (PC pump) consists of two major components, the rotor and the stator. The rotor, suspended by the rod string, is the downhole pump's only moving part. As the rotor turns within the stator, cavities are formed which progress from the inlet (bottom) to the outlet (top) of the pump (Figure1-1).

The definitions of some of the terms in Figure1-1 are as follows:

- Prime mover – An engine, usually natural gas, diesel, or electric, that provides power on a pumping unit.
- Wellhead – The top of the casing and the attached control and flow valves.
- Rod string – A length of sucker rods (steel rods that are 25 or 30 ft long and ½ in. in diameter that are screwed together and form the connection between the walking beam on a surface pumping unit and the downhole pump in an oil well.
- Production tubing – A small diameter tube (¾ to 4½ in. in diameter) that is suspended in a cased well. It is used to conduct the produced fluids to the surface.
- Stator – Vanes that direct fluid flow. The stators house the rotors and direct the fluid flow toward the rotors.

1.2. Pressure Pulsing Enhancement Technology

In this project, a pressure pulsing tool was used in the pulse well, so it is necessary to give a brief review of this technology. Pressure pulse flow enhancement is a relatively new physical phenomenon (Davidson et al., 1999; Samaroo, 1999). Conceptually, the hypothesis is based upon the existence of a tsunami-type (long period, low frequency,

high-amplitude) wave within a viscous fluid-saturated porous media subjected to appropriate large-strain excitation. This wave gives rise to a synergetic build-up of internal pressure within the pores of the media, under conditions of constant hydraulic head (Samaroo, 1999), which results in the enhancement of the fluid flow rate.

In the laboratory experiments, the sand matrix was made either immobile or allowed to flow (a simulation of cold production, although there was no gas dissolved in the oil phase). The excitation is obtained by hitting the exterior of the sand pack cell or the fluid with an impulse. The cell is packed with sand and heavy oil, which resembles the heavy oil reservoir, and a tube connects the cell with a water reservoir, which provides a constant pressure. For both immobile and mobile sand, pressure pulsing increased the fluid flow rate. In the field trial, the excitation applied to the porous medium is obtained by using a pressure pulsing tool, which is placed in a pulsing well surrounded by the production wells. The pulsing tool is designed to generate pressure pulses within the fluid contained in the reservoir. The relative locations of the pulsing well and the surrounding production wells in this project are shown in Figure2-1 of Chapter2.

1.3. Micro-Seismic Technique

Micro-seismic technique makes use of naturally occurring small earthquakes. In this technique, the seismic sources are naturally occurring fractures, with source position and origin times both unknown. In contrast, active seismic technique such as oil exploration uses artificial sources in which the source position and origin time are known precisely. This is why this technique is called ‘passive monitoring’.

1.3.1. Source Mechanisms

Micro-seismic events are very small earthquakes occurring on failure surfaces such as fractures. Because the earth stresses acting within a reservoir are deviatoric, shear stresses build up on naturally occurring fracture surfaces. Under normal conditions, these fracture surfaces are locked together. But when the in-situ stresses are changed by reservoir production activities, failure occurs on the fracture surfaces, and the micro-

seismic energy releases (Figure1-2). If a transducer is placed in the reservoir, micro-seismic signals can be recorded.

1.3.2. Application of Micro-Seismic Techniques

Seismicity is a very common phenomenon in underground mining. A seismic event in a given mine is often called a mine tremor, and only those seismic events that cause damage in accessible areas of the mine are called rock bursts. Out of several thousand seismic events recorded annually at some mines, only a few become rock bursts. Micro-seismic techniques are thus extensively used in the mining industry as an indication of rock bursts, which are very often the major cause of fatalities in mines. Rock bursts are violent failures of rock; they take place in the mining and geotechnical industries where large volumes of rock are excavated to create underground openings. During excavation, the removed rock mass no longer supports the stress produced by overlaying rock and tectonic movement; consequently, stress is redistributed around the opening of the excavation. This redistribution causes areas of high concentrated stress which may cause rock failure. Passive seismic monitoring technique provides a powerful means for the detection and evaluation of seismic events occurring around underground openings.

1.3.3. Data Analysis Techniques

The techniques used in the analysis of micro-seismic data include:

- **Event rate:** This parameter is used in mining for rock burst prediction by counting the number of events occurring in a certain time interval. Mining operations result in the removal of support from the mine structure, which in turn imposes new load-carrying requirements on the remaining structure. As the remaining structure adjusts to its new stress environment, small-scale displacements may take place. These displacement adjustments result in the release of seismic energy and seismic events can be recorded. Because stable areas of a mine structure release very few seismic events while unstable structures release large numbers of events, it is a useful tool to

record and analyze the event rate for analysis of the stability of a mine structure and thus predict rock bursts. (Hardy, 1977)

- Relative arrival times at several transducers: By recording the seismic events received at a set of transducers distributed around the source, its location can be determined.
- Focal mechanism: By studying the source moment tensor, the source type and the principal stresses may be determined.
- Strength of micro-seismic events: The magnitude and the seismic energy radiated are measurements of the strength of micro-seismic events.
- Direction of particle motion for P-wave: In a homogeneous and isotropic medium, the direction of particle displacements coincides with the direction of the P-wave propagation. Thus the direction of the source can be obtained by calculating the polarization orientation of the P-wave.

The first technique (event rate counting) is generally used in mining and the rest of these techniques will be discussed in detail in Chapter4.

1.4. Micro-Seismic Techniques in Cold Heavy Oil Production

1.4.1. Purposes of Applying Micro-Seismic Techniques to Cold Heavy Oil Production

Monitoring the Production Process of the Well

One of the purposes of using micro-seismic techniques in CHOP is to monitor the sand production. In cold production wells, one problem caused by sand production is that when the sand and oil mixture flows into the well, the sand always settles on the top of the pump rotor, which results in a high pump-motor torque and may result in the pump damage when the torque is too high. With the micro-seismic data recorded during the production process, high pump torque can be detected immediately or even be predicted, so procedures can be taken to prevent the pump damage.

Monitoring the Operation of the PC Pump and the Pulse Tool

The micro-seismic signatures of the PC pump change significantly during periods of abnormal operation. Also any damage or breakage of the pulse tool will create seismic signals, which are distinct from other signals. Thus the micro-seismic data is able to act as an abnormal operation indication.

Acquiring Information About the Medium Properties

Information of the connectivity of the reservoirs may be obtained from the small seismic events taking place in the reservoir. In this project, the cap rock is shale, and one of the sources of the seismic signals is the shale failure above the yielded sand. Sometimes the shale may fall down into the reservoir and block an area thus making the area impermeable. When an impermeable area exists in the sand between the source and the receiver, the seismic signals received may have different features from those propagating in a pure sand medium, due to the possible reflection at the impermeable surface.

1.4.2. Micro-Seismic Activities in Cold Heavy Oil Production

The micro-seismic activities in this project are comparable to those in mines. The dominant activities can be summarized as below:

- Shale failure at the shale-sand interface: As the sand moves away with the oil, the yielded zone becomes lower in density, and the sand matrix is no longer able to support the stress from the cap rock, shale, so the shale fails, and creates seismic signals propagating outward.
- Sand failure at the boundary between the intact reservoir and the yielded zone (foamy zone): As mentioned above, there is a density difference between the foamy zone and the intact reservoir. Due to this difference, stress builds up on their boundary. Sand failure may occur on this boundary. However, there is some dispute over this point. Some contend that seismic activity in the sand is unlikely.
- Other seismic events caused by production activities: These events may include the events caused by the pulse tool operation, the mechanical failure of the pulse tool or the abnormal operation of the PC pump.

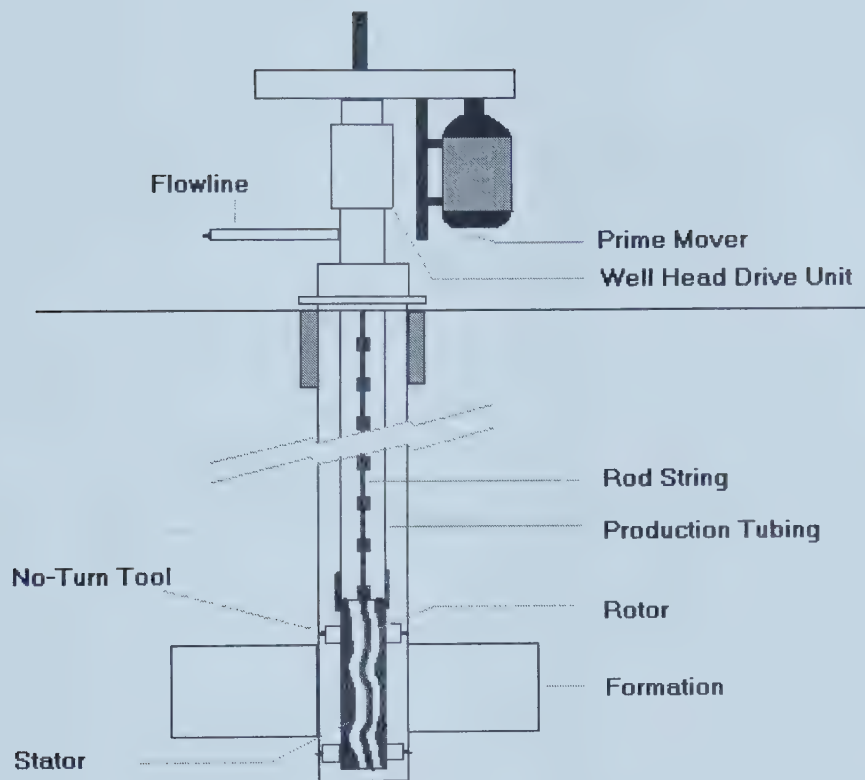


Figure1-1 Configuration of a typical CHOP well.

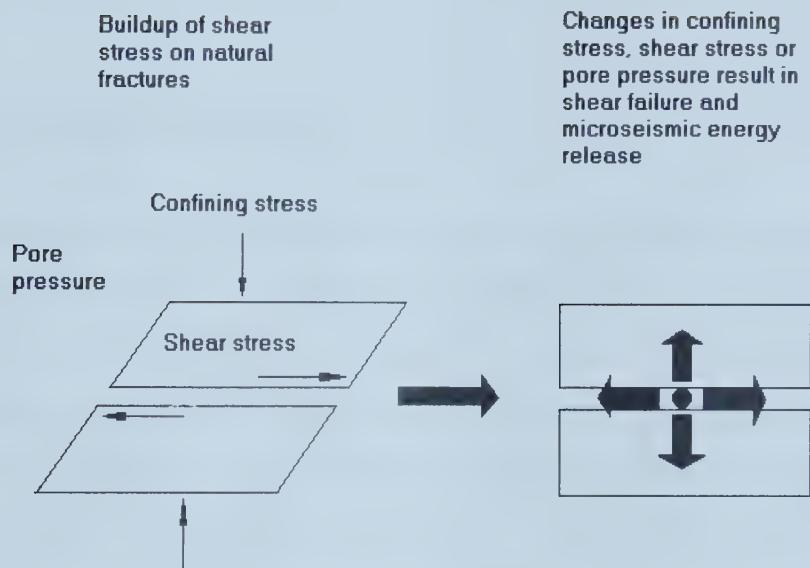


Figure1-2 Conceptual schematic showing typical micro-seismic source mechanisms (Jupe, 1998).

2. Geology and Reservoir Setting

In this project, the wells in which micro-seismic monitoring and continuous pressure pulsing were applied during the period September to December 1998, was located in Wascana Energy Limited's Luseland, Morgan and Plover Lake Fields. These fields are situated in a common geological setting, which is the Mannville Group of channel sands.

2.1. The Mannville Group of Sands

The Mannville Group of sands is an extensive group of sands that are found in West-central Saskatchewan and East-central Alberta. The Lloydminster Play covers approximately 256,000km² of this region and comprises various geological formations that contain heavy oil (12-23°API) within the Mannville Group (MacCallum, 1981). (°API is an arbitrary scale expressing the gravity or density of liquid oil products devised jointly by the American Petroleum Institute and the United States National Bureau of Standards. The measuring scale is calibrated in terms of degrees API gravity. Crude oil with the least specific gravity has the highest API gravity. The formula for determining API gravity is as follows: $\text{API gravity} = (141.5/d) - 131.5$, where d is the specific gravity at 15.6° C. Fresh water has 10 °API. Crude oils generally range from 6°API (very heavy) to 60°API (very light). Average oils range from 35°API to 25°API. Light oils range from 35° to 45° and heavy oils are less than 25° API.)

The Mannville Group within the Lloydminster area has been determined to be of Lower Cretaceous age. It consists of a series of poorly consolidated (uncemented), interlaminated sandstones, shales and coals overlying a Paleozoic unconformity. The unconformity is overlain by shales of the Joli Fou Formation, and has a regional dip of 2m/km to the southwest (Dunning et al., 1980). The Mannville Group has been further subdivided into nine fluvio-depositional and coastal members within the Lloydminster area, on the basis of electrical log characteristics (Samaroo, 1999). These are (from the base upward) the Dina, Cummings, Lloydminster, Rex, General Petroleum (GP), Sparky, Waseca, McLaren and Colony. The composition and depositional history of this

group is complex, and this complexity was created by variations in sediment source and depositional environment. The Dina, Lloydminster, Sparky and GP members are composed of sediments derived dominantly from the Pre-Cambrian Shield to the north and east. The Cummings, Rex, Waseca, McLaren and Colony members consist of sediment derived dominantly from the Cordillera to the west (Samaroo, 1999).

The Dina member is typically coarse-grained quartz sandstone deposited in a fluvial environment on the Paleozoic unconformity. The Cummings, Lloydminster, Sparky and GP members were deposited in marine to near-shore marine environments in cyclical sequences reflecting the transgressive and regressive phases of the Boreal and Gulfian Seas of Lower Cretaceous age (Dunning et al., 1980). While sediments within the Rex are largely of marine to near-shore marine, some continental deposits have been recognized in this member as well.

The Waseca, McLaren and Colony sands comprise the 'upper' Mannville sands. Distribution of these sands reflects local variations in sedimentary depositional environments, and is difficult to correlate them spatially across the region. Evidence suggests that these sands were most likely deposited in an extremely flat continental-fluvial environment (Dunning et al., 1980). The Waseca member is generally thicker than the other members of the Middle to Upper Mannville (Lloydminster and Colony) are. Organic-rich clastic sediments and coal overlain by shales and silts generally define the interface between the Sparky and the Waseca. The Waseca is generally overlain by the 'lower' McLaren, which typically grades upward from a shale to a clean sand and may have originated from a pro-grading tidal or deltaic environment. Dunning et al reports that this gradational character is also recognized in the 'middle' Mannville GP and Sparky members as well.

The Mannville Group of Sands can thus be described as a high porosity (generally ~30%) and permeability (generally >500 mD, and usually >1 D) geological sandstone sequence sandwiched with shales, silt and coal. Lack of lateral continuity of the individual members of the formation, erosional channels infilled with low permeability silt or other material and random interspersed shales present barriers to fluids migration. This leads to isolated or semi-isolated pools of hydrocarbons within the larger reservoir system. Similarly, erosional channels in low permeability material infilled with sands

may also provide hydrodynamic continuity and pathways for preferential fluid migration and accumulation within low permeability sections of strata.

The wells in this section exploit mainly the Sparky Sands. The geologic attitude of the reservoir is relatively flat within the section. The average thickness of the Sparky Sands ranges from a maximum of about 7 meters at the location of well 7B-36 (the pulsing well, where the pressure pulsing tool was located) to a minimum of about 1 meter on the eastern and southern regions of the section. This is shown in Figure2-1.

2.2. The Standard Heavy Oil Well on Cold Production

Typical heavy oil wells drilled in the Lloydminster region are completed with a seven-inch (175mm) casing cemented in place and then perforated with extra big-hole charges (~18-25mm) in the upper level of the oil-saturated zone. Because of the critical need to continuously produce formation sand to achieve economic production rates, heavy oil wells do not use filters or gravel packs around or within the perforated fluid intake zone (which is the case in a conventional oil well). A diagram of the typical heavy oil well is shown as Figure1-1.

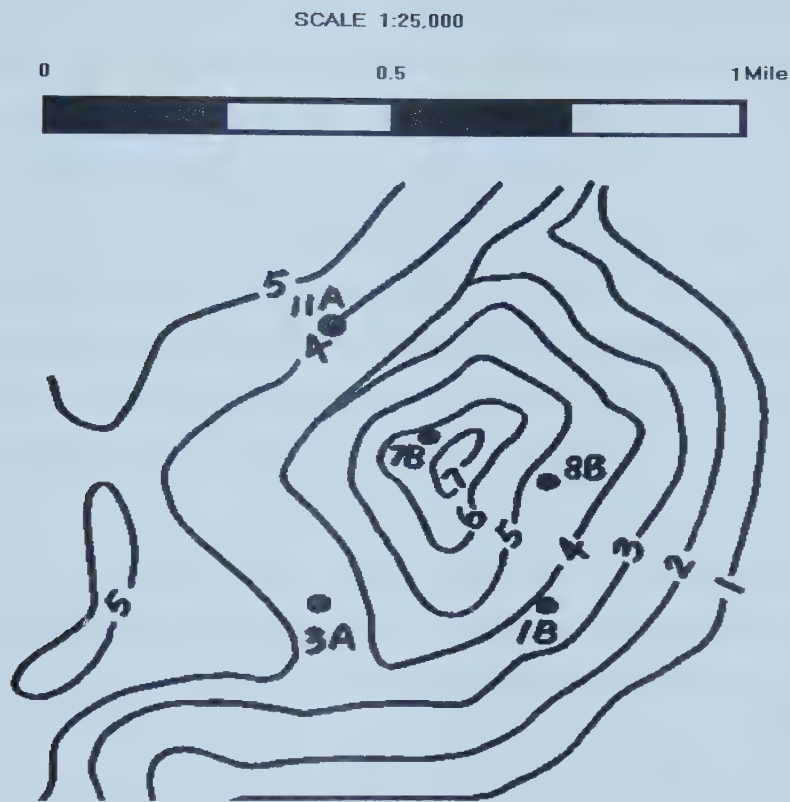


Figure2-1 A map showing the interpolated Sparky Sand thickness derived from well logs (Samaroo, 1999). The numbers are sand thickness in meters. Only the wells used in this project are shown in this figure among which 7B is the pulsing well and the others are the monitoring wells.

3. Instrumentation and Data Collection

The application of the pressure pulse excitation in a fluid-saturated reservoir would result in the increase of the pore fluid pressure and micro-seismicity resulted from sand-shale destabilization or slippage along induced yielding surfaces within the reservoir. Perturbations and increases in pore pressure should trigger stick-slip yielding in the regions that are the closest to the critical stress conditions.

The instrumentation required for detection of these stick-slip events consisted of high-sensitivity triaxial piezo-crystal accelerometers. There were four accelerometers originally installed in the four monitoring wells, respectively. Installation of the instrumentation within the reservoir being stimulated was determined to be vital for detection of reliable signals. This would avoid problems of reflection and channeling of seismic energy because of impedance contrasts between the reservoir and the surrounding rocks (Nyland and Dusseault, 1983). Special instrumentation packages were designed which allowed the placement of a triaxial accelerometer on the end of the production tubing string within the monitored producing wellbore. Excitation and responses from these devices were conveyed from the downhole instrumentation to uphole recording and excitation systems via armored wireline cables.

3.1. Downhole Instrumentation

The accelerometers selected were hermetically sealed piezoelectric sensors incorporating built-in microelectronics requiring constant-current excitation signals. These sensors have a measurement range of $\pm 5g$ -peak acceleration, and are capable of a broadband resolution of $60 \mu g$ (Samaroo, 1999).

The accelerometers on the monitoring wells were mounted on 'belly spring' centralizers that were semi-rigidly fastened onto the end of the instrument pack. This method of attachment allowed for some movement of the accelerometer-mount unit in the vertical plane, but minimal movement in the horizontal (rotational) plane. The flexibility of the 'belly spring' unit allowed the accelerometer to be firmly pressed against the interior wall of the well casing. This assembly is shown in Figure3-1.

For the four monitoring wells, the accelerometer elevations were:

- **Well 1B-36** – The accelerometer was positioned at 537.84mKB within the interval of open perforations of the Sparky Sands (536.5-540mKB). (mKB: distance in meters from the Kelly bushing. The Kelly bushing is a device fitted to the rotary table. The rotary table is a heavy, circular casting mounted on a steel platform just above the derrick floor with an opening in the center through which the drill pipe and casing must pass.) (Perforations: Holes shot in the casing or liner, cement, and producing formation by bullets or shaped-explosive charges to allow oil and/or gas from a producing zone to flow into the well.) The bottom of the slotted PC pump intake on this well was positioned at an elevation of 536mKB. The bottom of the no-turn tool was located at a depth of 536.59mKB. The bottom of the perforated pup joint (secondary pump intake) was placed at a depth of 537.29. With this arrangement, only the secondary pump intake is located within the perforations of this well and it utilizes only the upper 23% of the perforated interval.
- **Well 3A-36** – this well has two active perforations within the Sparky Sands. The first set of perforations is located between 538.5-540.5mKB and the second set is located between 543.5-544.5mKB. The accelerometer on this well was positioned at 543.94mKB. The slotted (main) intake of the PC pump was positioned at 542.05-542.55mKB. The no-turn tool was located at 542.78-543.32mKB and the secondary intake of the PC pump (perforated pup) was located at 543.32-544.01mKB.
- **Well 8B-36** – This well also has two active perforations within the Sparky Sands. The uppermost perforations are located at 544-546mKB and the lower set at 547.75-550.5mKB. The accelerometer was placed at 548.84mKB. The slotted intake of the PC pump was placed at 546.35-546.85mKB. The no-turn tool was located at 547.08-547.63mKB while the secondary pump intake was placed at 547.63-548.38mKB.
- **Well 11A-36** – This well was perforated twice in the Sparky Sands. The first perforation level is 558-560.3mKB, and the second is 561.5-565mKB. The primary PC pump intake was located at 556.35-556.85mKB. The no-turn tool is located at

557.08-557.64mKB. The secondary pump intake (perforated pup joint) is located at 560.82-561.52mKB. The location of the accelerometer in this well is 562.01mKB.

The accelerometers (and pressure transducers) in all of the monitoring wells were located within the active perforations (or the lowermost of the active perforations, when there is more than one perforated interval). Armored wireline cable was used to connect the downhole instrumentation to the surface excitation and recording systems (Samaroo, 1999).

3.2. The Recording (ISS) Systems

Each recording unit consisted of a standard International Seismic Systems Micro-seismic analog-to-digital converter assembly (MS box) linked to a Pentium I-166 MHz CPU through a Motorola GPS receiver-timing unit. Each MS box comprised of an analog-to-digital electronic interface card wired to provide excitation to the downhole accelerometer and to receive the response signals provided by this device. These response signals were assigned an absolute time by the GPS receiver unit and then stored on the hard drive of that unit's CPU. The corresponding ISS runtime software allowed configuration of the micro-seismic trigger levels as well as initial viewing of the waveforms recorded. The configuration of the seismometers permitted reception of both triggered events, at digital sampling rates of 16kHz and buffer length of 4 seconds, and collection of continuous background micro-seismicity at sampling rates of 10Hz and buffer length of 8 minutes.

3.3. Downhole Seismic Data

Reliable downhole seismic data was generated by one station on well 8B-36, since the electrical continuity of the other three accelerometers was lost after placement of the equipment downhole. The data consisted of triggers of magnitude above the average background noise and continuous eight-minute averages of the background noise.

3.3.1. Average Continuous Monitoring Background Seismicity

Each average continuous monitoring record consists of approximately eight minutes of discrete sampling of the seismicity within the wellbore and reservoir. These samples were taken continuously throughout the monitoring period and recorded as the average seismic background noise. Each eight-minute record was then merged with all of the other records for that day to produce a seismic record for that day to provide a day's average background seismicity.

The average background noise of the pump and the reservoir was detected and this noise level is constant unless there are changes in the pump's operation or external triggers. An average background noise created by the PC pump and the reservoir under normal condition is shown in Figure3-2.

Triggered seismic events are also recorded on the average continuous monitoring record, and these are shown as anomalies ('spikes') above the background level (Figure3-3). Some of these major anomalies are assumed to be due to sand or shale failures within the reservoir.

Such failure generally leads to a change in the average background noise of the PC pump, generating what seems to be resonance or a low-frequency semi-rotational wobble. This change in behavior seems to be consistent with the application of high torque to a pump under high load and the frequency of the wobble appeared on the average background noise is believed to be consistent with that of the pump moving the high sand-content fluid. Application of high levels of rotational torque to a bottom-hole pump under high load through a 600m long drive rod may likely lead to changes in the vibrations detected on the accelerometer. This behavior is thus consistent with the generation of sand slugs entering the wellbore. The triggers detected could possibly be failures of shale bands or collapse of sand at the crumbling zone, leading to the generation of a sand slug traveling to the well bore (zone of lower pressure). The PC pump would require higher torque to remove this high-sand content fluid from the wellbore, which may lead to the changes in background signature observed. Figure3-4 shows an example of the change in background noise of the PC pump recorded after a recorded event.

3.3.2. Triggered Seismic Events

Triggered seismic events were observed to consist of four different waveforms:

- a) Tube wave generated by gas within the wellbore (Figure3-5): Wellbore gas production was discovered to be highly irregular. This is probably due to buildup of gas pressures outside of the wellbore, near the perforations, until an entry pressure is achieved. This would result in bursts of gas entering the well, generating small-scale seismic events and creating tube waves that would propagate vertically within the well. This triggered event may also have been generated by accumulation of gas within the wellbore under a diametrical constriction such as the no-turn tool. Such a phenomenon would also result in the buildup of gas pressures until it achieves a critical breakout pressure, which would generate vertically oriented tube waves.
- b) Events generated by the pulse well (Figure3-6 and 3-7): Failure of the hydraulic braking mechanisms on the pulse tool on January 9, 1999 resulted in direct contact of part of the falling (metallic) pulse-plunger section with the wellhead. A considerable amount of triggered events of a distinct waveform was received during the period when this fault existed on the pulse tool. These triggers were only received during this period, and ceased after the pulse tool was fixed.
- c) A sharp P-wave propagating in a homogeneous medium (Figure3-8)
- d) A diffuse P-wave: One possible reason for the disperse P-wave observed in some records could be a P-wave propagating in an inhomogeneous medium (Figure3-9): Triggered waveforms of the type shown in Figure3-8 and 3-9 were consistently received throughout the duration of the pulsing project, with a higher incidence of these waveforms being received after the commencement of pulsing.

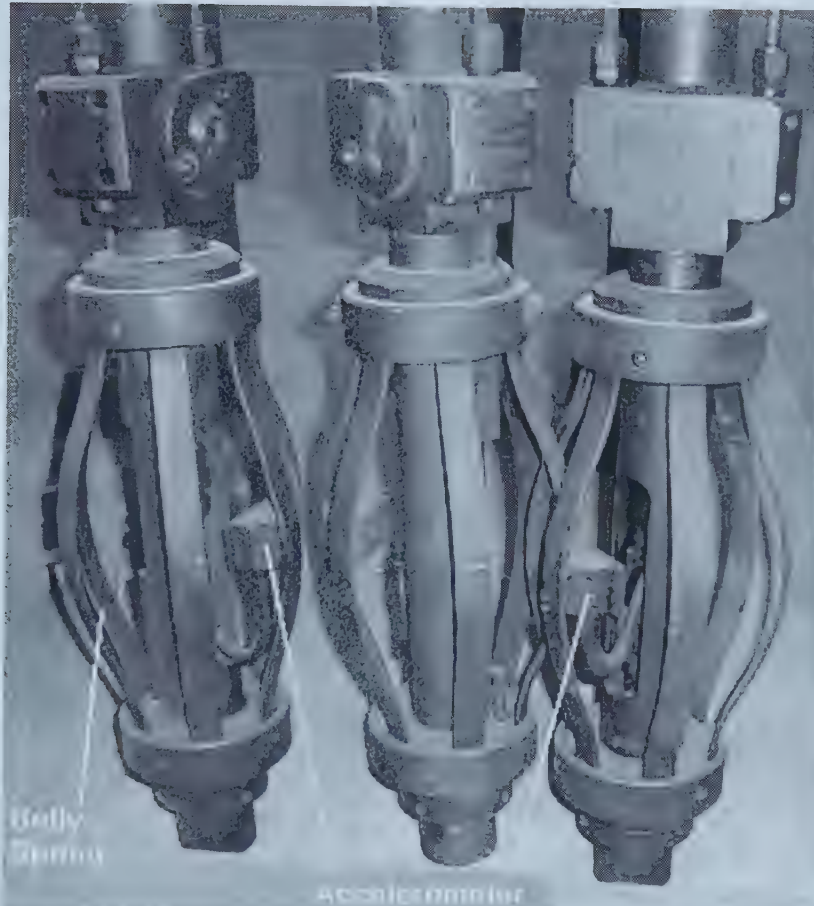


Figure3-1 Mounted accelerometers on 'Belly Spring' assembly.

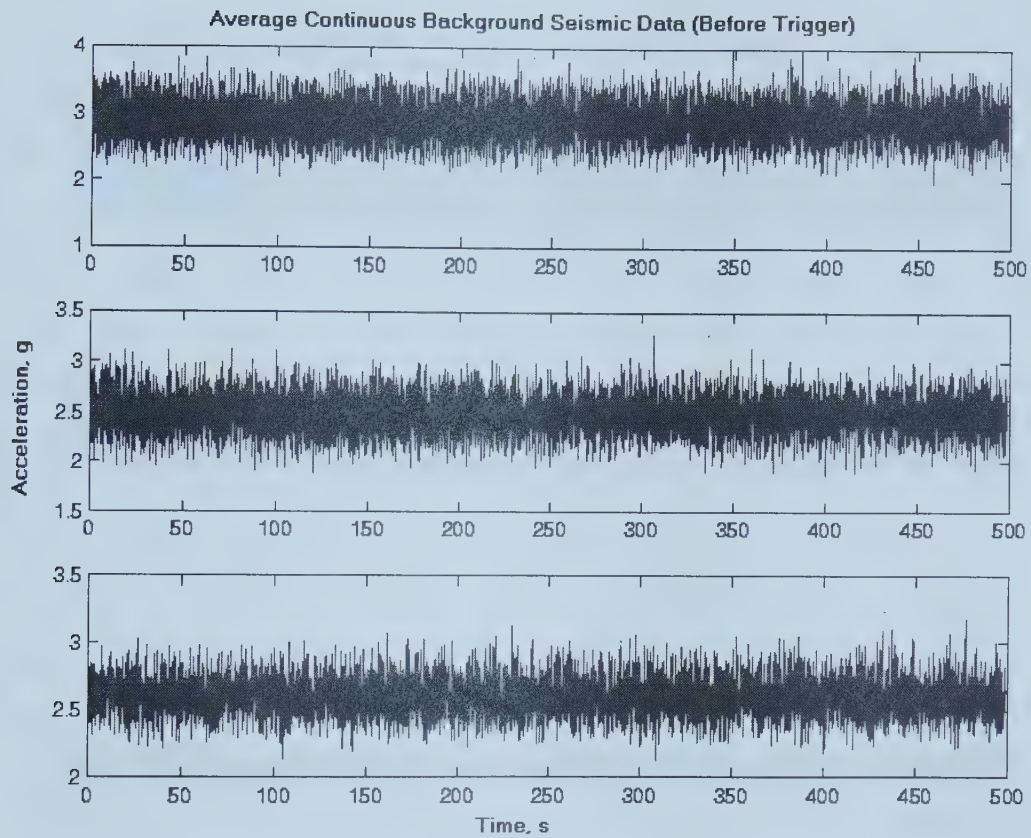


Figure3-2 Average background noise created by the PC pump and the reservoir under normal condition. The three panels from top to bottom are the vertical, radial and tangential components, respectively.

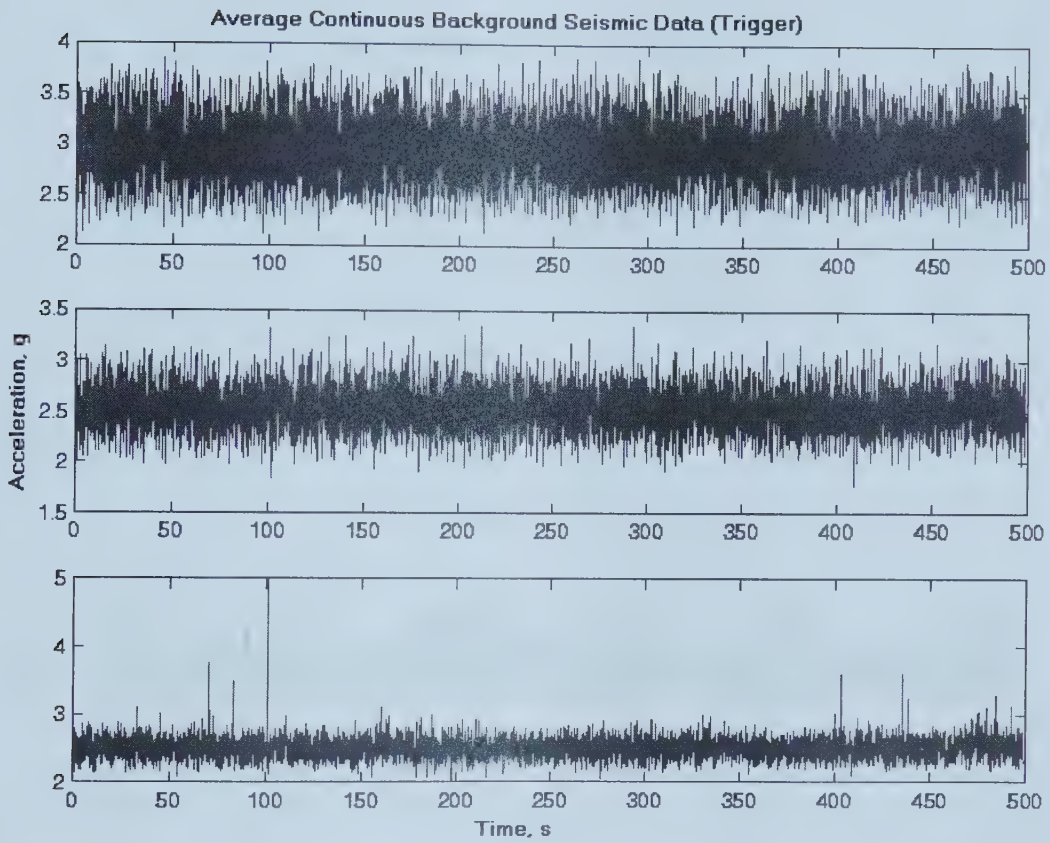


Figure3-3 Triggered seismic events recorded on the average background noise. The three panels from top to bottom are the vertical, radial and tangential components, respectively. The spikes appeared on the bottom panel are assumed to be caused by triggered seismic events. They appear as spikes due to the very short duration time (about 0.01s).

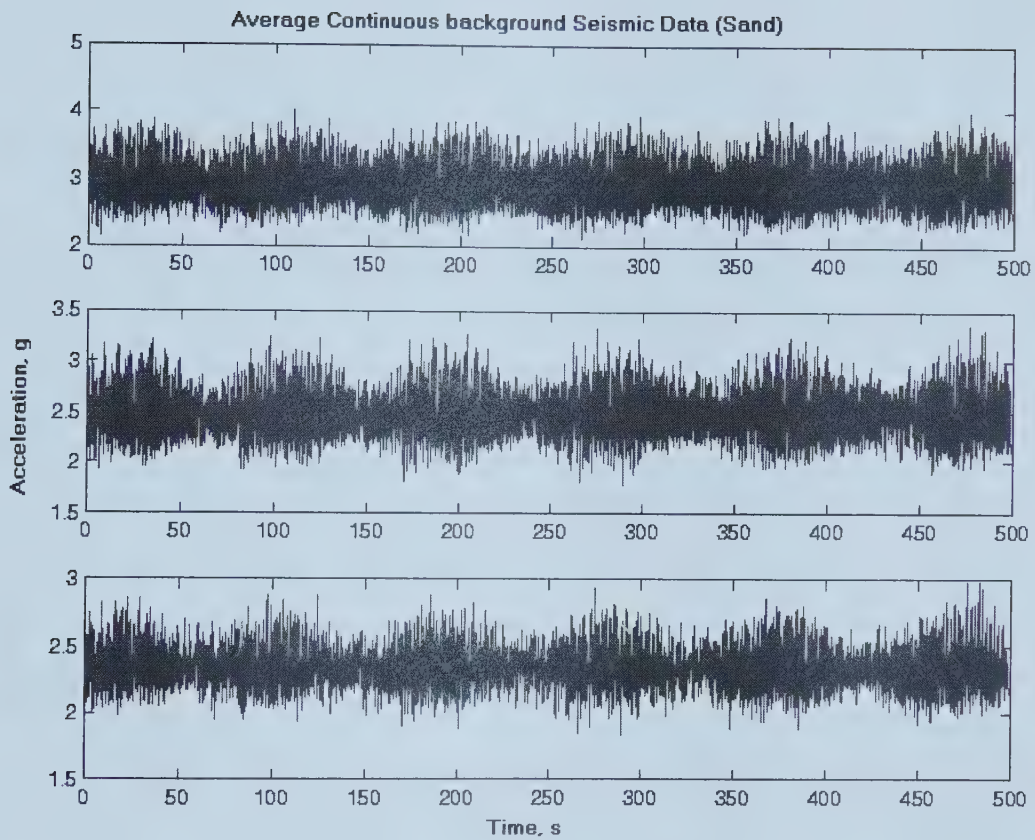


Figure3-4 Average background noise indicating sand coming into the well bore. The three panels from top to bottom are the vertical, radial and tangential components, respectively. The wobbles on the three panels are associated with sand production and the frequency of the wobbles is assumed to be consistent with the speed of the pump motor.

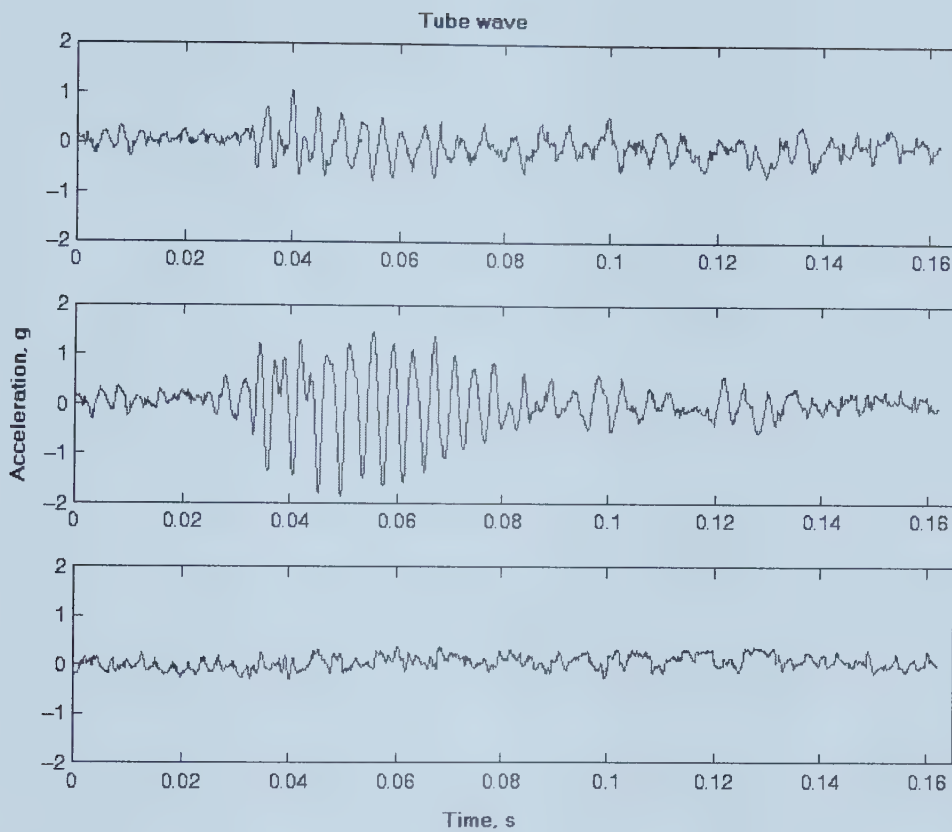


Figure3-5 Tube wave generated by gas. The three panels from top to bottom are the vertical, radial and tangential components, respectively. The tube wave appears only on the first two panels, since it is a elliptically polarized surface wave with a vertical and a horizontal components.

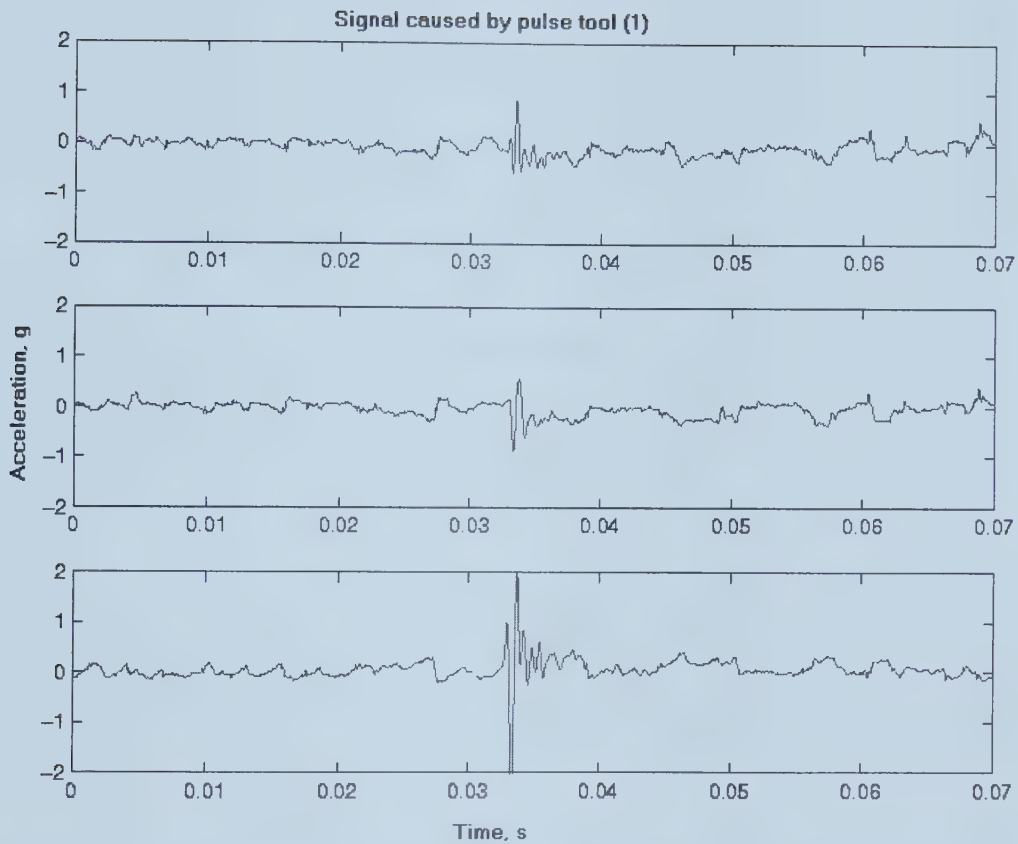


Figure3-6 Event generated by the pulse well due to failure of the hydraulic braking mechanisms on the pulse tool. The three panels from top to bottom are the vertical, radial and tangential components, respectively. The events in this figure and in Figure3-7 are of the same type. These types of event were received when the failure existed on the pulsing tool; they were no longer received after the tool was fixed.

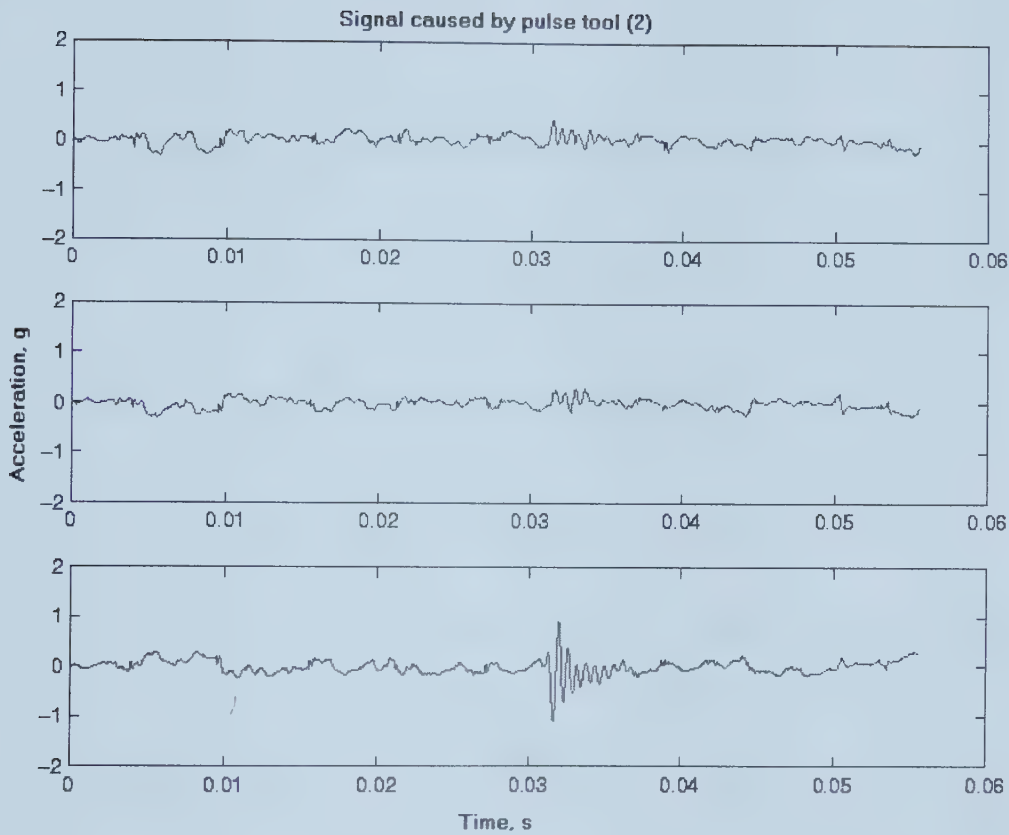


Figure3-7 Event generated by the pulse well. The three panels from top to bottom are vertical, radial and tangential, respectively. Since the pulse tool was installed in the well 7B-36 while the monitoring accelerometer was in the well 8B-36, the clear waveforms received indicate that the reservoirs in this region are connected. Otherwise if a fault exists between the two wells there would be a strong reflection interface so that much of the energy of the seismic waves would be reflected and very little could transmit through the medium to the accelerometer.

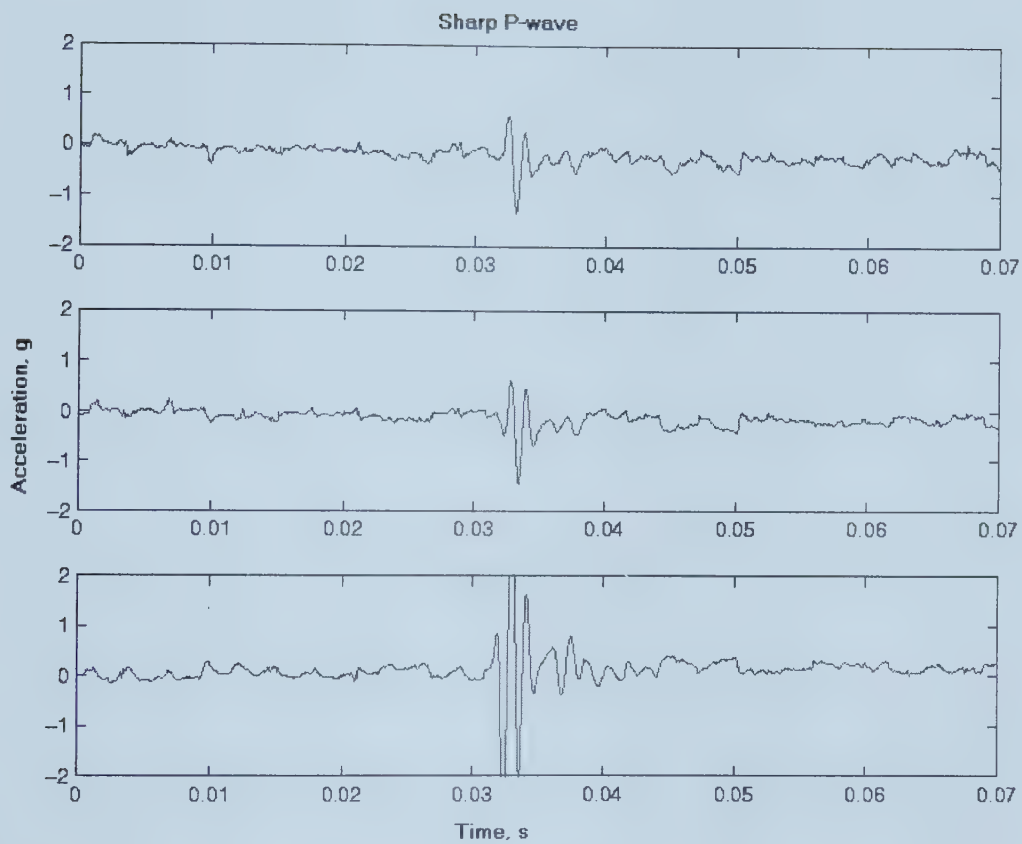


Figure3-8 A sharp P-wave propagating in a homogeneous medium. The three panels from top to bottom are vertical, radial and tangential, respectively.

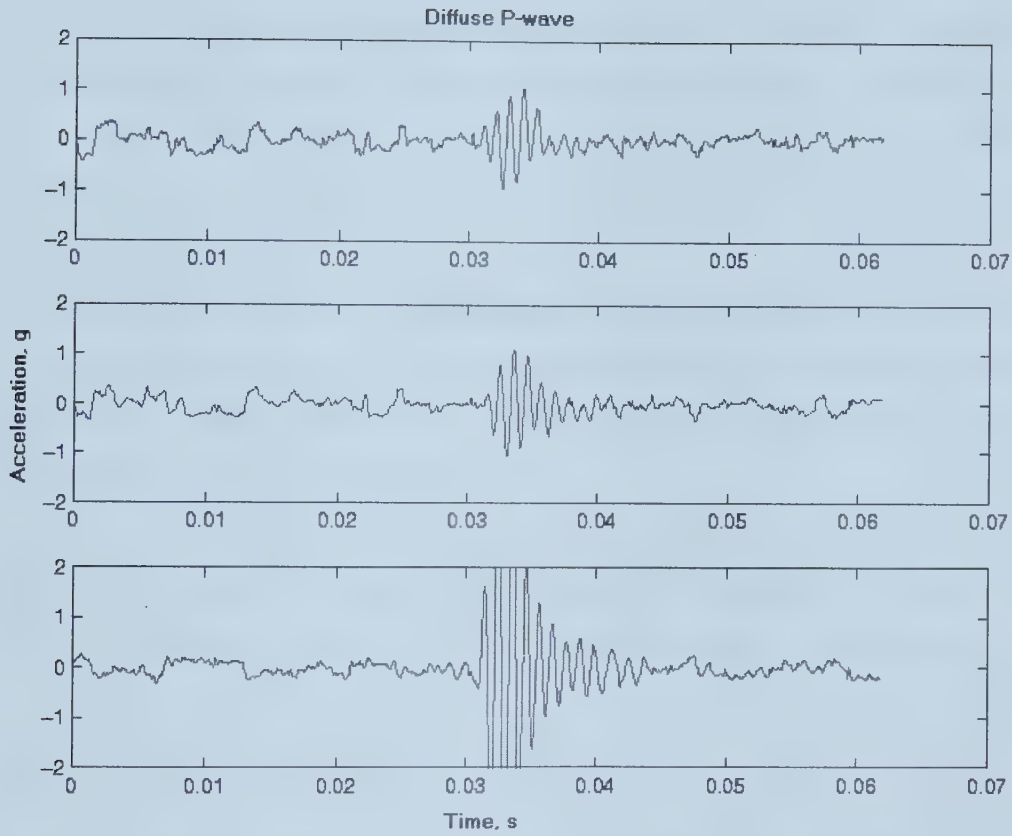


Figure3-9 A diffuse P-wave which is assumed to have propagated through an inhomogeneous medium. The three panels from top to bottom are vertical, radial and tangential, respectively.

4. Data Analysis

4.1. Source Location

Location of seismic events is the first step in studies of naturally occurring seismicity. Source location of a seismic event is only possible when data is available from an array of receivers. With a minimum of three receivers, source location on a horizontal plane (epicenter) can be determined but with depth unknown. To determine the depth of the source (hypocenter), one more receiver is needed.

Usually the origin time and focal depth of the source are of secondary importance and may be estimated crudely. For a densely distributed group of recording stations, the first *P*-arrivals at these stations can be used to construct a time contour, and the earliest possible time on the contour is the epicenter.

If both *P*- and *S*-arrival times are available, the difference between *S*- and *P*-arrival times can be used to obtain a rough estimate of the epicenter. With at least three stations, the distance *D* from the source to each station can be expressed as

$$D = [V_P V_S / (V_P - V_S)] / (T_S - T_P), \quad (4.1-1)$$

Where V_P and V_S are the *P*- and *S*- wave velocities and T_P , T_S the *P*- and *S*-arrival times. Then the epicenter may be placed at the intersection of circles with the stations as centers and *D* as radii. The intersection will seldom be a point. This method can only give a rough estimate of the source area. However, it cannot be used in the present case since there is no *S*-wave received due to the suspension form of the matrix (the matrix cannot support shear stress).

To get a more accurate source location, the hypocenter, at least five receivers are used when the errors included in the data are considered. The various locating approaches are based on the criterion of different treatment of time residuals. For a given velocity model a time residual is defined as the difference between the observed and theoretical arrival time of a seismic wave. In the first type of approach, the time residuals are considered regardless of their causes (represented by the classic least squares approach)

while in the second type the time residuals are divided into two components: time residuals caused by reading errors of arrival times and those caused by velocity uncertainties (such as the Fedorov's approach and the relative location approach).

4.1.1. The Classic Least Squares Approach

The classic least squares approach is a type of locating approach that does not differentiate the causes of time residuals. The problem is described as: Given n observations of arrival times t_1, t_2, \dots, t_n at n stations, find the origin time t_0 and the hypocenter (x_0, y_0, z_0) , such that the sum of squared time residuals r_i ,

$$\Phi(t_0, x_0, y_0, z_0) = \sum_{i=1}^n r_i^2, \quad (4.1-2)$$

becomes minimum, where r_i is equal to $t_i - t_0 - T_i(x_0, y_0, z_0)$. $T_i(x_0, y_0, z_0)$ is the calculated travel times from the hypocenter to station i , and $t_0 + T_i(x_0, y_0, z_0)$ is the theoretical arrival time at station i .

An iterative procedure is applied in this approach. At the beginning of the iteration, an estimated source parameter, the initial values of the source location and origin time, θ^* , is used according to the known information of the micro-seismicity in the area studied. So

$$\begin{aligned} \theta^* &= (t_0^*, x_0^*, y_0^*, z_0^*)^T \\ \mathbf{t} &= (t_1, t_2, \dots, t_n)^T \\ \mathbf{T}(\mathbf{h}^*) &= (T_1(h^*), T_2(h^*), \dots, T_n(h^*))^T \\ \mathbf{h}^* &= (x_0^*, y_0^*, z_0^*)^T \end{aligned} \quad (4.1-3)$$

where \mathbf{t} is the observed arrival times at n stations and \mathbf{h}^* is the initial hypocenter coordinates. The theoretical travel time from this estimated source to station i , $T_i(h^*)$, is calculated as

$$T_i(h^*) = [(x_i - x_0^*)^2 + (y_i - y_0^*)^2 + (z_i - z_0^*)^2]^{\frac{1}{2}} / v \quad (4.1-4)$$

The time residual at θ^* , Δt^* , is expressed as

$$\Delta t_i^* = t_i - t_0^* - T_i(h^*) \quad (4.1-5)$$

Assume $\delta\theta$ is the correction to θ^* , and $\delta\theta = (\delta t_0, \delta x_0, \delta y_0, \delta z_0)^T$, so the new source after correction will be $\theta^{**} = (t_0^{**}, x_0^{**}, y_0^{**}, z_0^{**})^T$, which is equal to

$$\begin{aligned} \theta^{**} &= \theta^* + \delta\theta \\ &= (t_0^* + \delta t_0, x_0^* + \delta x_0, y_0^* + \delta y_0, z_0^* + \delta z_0)^T. \end{aligned} \quad (4.1-6)$$

The new travel time for θ^{**} , $T_i(h^{**})$, is

$$\begin{aligned} T_i(h^{**}) &= T_i(h^* + \delta h) \\ &= [(x_i - x_0^* - \delta x_0)^2 + (y_i - y_0^* - \delta y_0)^2 + (z_i - z_0^* - \delta z_0)^2]^{\frac{1}{2}} / v, \end{aligned} \quad (4.1-7)$$

where $\delta h = (\delta x_0, \delta y_0, \delta z_0)^T$. Applying the first order Taylor expansion of $T_i(h^* + \delta h)$,

$$T_i(h^* + \delta h) = T_i(h^*) + \delta x_0 \partial T_i(h^*) / \partial x_0 + \delta y_0 \partial T_i(h^*) / \partial y_0 + \delta z_0 \partial T_i(h^*) / \partial z_0. \quad (4.1-8)$$

The time residual for the corrected source θ^{**} , r_i , is described as

$$\begin{aligned} r_i &= \Delta t^{**} \\ &= t_i - t_0^{**} - T_i(h^{**}) \\ &= t_i - t_0^* - \delta t_0 - T_i(h^*) - \delta x_0 \partial T_i / \partial x_0 - \delta y_0 \partial T_i / \partial y_0 - \delta z_0 \partial T_i / \partial z_0 \\ &= \Delta t^* - \delta t_0 - \delta x_0 \partial T_i / \partial x_0 - \delta y_0 \partial T_i / \partial y_0 - \delta z_0 \partial T_i / \partial z_0 \end{aligned} \quad (4.1-9)$$

The problem is to find proper values for δt_s , δx_0 , δy_0 and δz_0 so that the squared time residual r_i^2 at the corrected source is minimum. Writing equation (4.1-9) in matrix form,

$$\mathbf{r} = \Delta \mathbf{t} - \mathbf{A} \delta \boldsymbol{\theta} \quad (4.1-10)$$

where \mathbf{r} is the time residual after the correction of $\delta \boldsymbol{\theta}$, $\Delta \mathbf{t}$ is the time residual before correction and \mathbf{A} is expressed as

$$\mathbf{A} = \begin{bmatrix} 1 & \partial T_1 / \partial x_0 & \partial T_1 / \partial y_0 & \partial T_1 / \partial z_0 \\ \vdots & \vdots & \vdots & \vdots \\ 1 & \partial T_n / \partial x_0 & \partial T_n / \partial y_0 & \partial T_n / \partial z_0 \end{bmatrix}. \quad (4.1-11)$$

The problem of minimizing $\sum_{i=1}^n r_i^2$ then becomes minimizing $\mathbf{r}^T \mathbf{r}$ by choosing a suitable $\delta \boldsymbol{\theta}$. Let $\hat{c}(\mathbf{r}^T \mathbf{r}) = \hat{c}(\delta \boldsymbol{\theta})$ equals zero, i.e. $\hat{c}(\Delta \mathbf{t} - \mathbf{A} \delta \boldsymbol{\theta})^T (\Delta \mathbf{t} - \mathbf{A} \delta \boldsymbol{\theta}) = \hat{c}(\delta \boldsymbol{\theta})$ equals zero, the following expression for solving for $\delta \boldsymbol{\theta}$ is obtained:

$$\delta \boldsymbol{\theta} = (\mathbf{A}^T \mathbf{A})^{-1} \mathbf{A}^T \Delta \mathbf{t}, \quad (4.1-12)$$

and $\delta \boldsymbol{\theta}$ is then added to the previous source parameters and a new iteration begins until some termination criteria is met (the adjustments or the root-mean-square value of the time residuals falls below some prescribed value, or if the allowed number of iterations is exceeded).

The above calculations are based on the assumption that the reliability of all observed arrival times t_1, t_2, \dots, t_n is the same. If some arrival times are considered more reliable than the others, the procedure must be modified to a weighted form. The misfit function $\Phi(\boldsymbol{\theta})$ is then equal to the weighted sum of the squared time residuals and takes the form

$$\Phi(\boldsymbol{\theta}) = \mathbf{r}^T \mathbf{C}_r^{-1} \mathbf{r}, \quad (4.1-13)$$

and the solution for the source correction, $\delta\theta$, is

$$\delta\theta = (\mathbf{A}^T \mathbf{C}_r^{-1} \mathbf{A})^{-1} \mathbf{A}^T \mathbf{C}_r^{-1} \Delta \mathbf{t} \quad (4.1-14)$$

where \mathbf{C}_r is the diagonal matrix $\mathbf{C}_r = \text{diag}(\sigma_{r1}^2, \dots, \sigma_{rn}^2)$, and σ_{ri} is the standard deviation of time residuals at station i . Let $\Delta \mathbf{t}' = \Delta \mathbf{t} \mathbf{C}_r^{-1/2}$ and $\mathbf{A}' = \mathbf{A} \mathbf{C}_r^{-1/2}$, equation (4.1-14) will take the same form as (4.1-12):

$$\delta\theta = (\mathbf{A}'^T \mathbf{A}')^{-1} \mathbf{A}'^T \Delta \mathbf{t}'. \quad (4.1-15)$$

Other problems may sometimes exist with the iterative classic least squares approach. One is the influence of a poor initial hypocenter parameter θ^* . Since the travel times $T_i(h)$ are usually quadratic, more than one minimum of the misfit function $\Phi(\theta)$ may exist. If the initial value of θ^* is poorly chosen, the iteration may terminate at a local minimum, which is not the lowest point of Φ (the global minimum). To solve this problem, several starting points θ^* can be tried in a feasible range and ascertain whether they all provide the same minimum value of Φ . Another problem rises when the matrix $\mathbf{A}^T \mathbf{A}$ is singular or near singular. The least squares solution of equation (4.1-12) can always be found if the matrix $\mathbf{A}^T \mathbf{A}$ is nonsingular. As $\mathbf{A}^T \mathbf{A}$ becomes near singular, the corrections $\delta\theta$ oscillate and become very large, leading to instability and divergence of the iteration procedure. However, this problem can be solved by some procedures that reduce the condition number (an estimate of the relative error in the solution) of this matrix (Gibowicz and Kijko, 1994)

4.1.2. Fedorov's Generalization of Least Squares Procedure

In this approach the time residuals are divided into two parts: the part caused by measurement error of arrival times and the part caused by velocity uncertainties. Still

the misfit function $\Phi(\boldsymbol{\theta}) = \mathbf{r}^T \mathbf{C}_r^{-1} \mathbf{r}$ is used in the least squares iteration procedure to acquire the correction of source parameters $\delta\boldsymbol{\theta}$. The only difference from the classic procedure is the treatment of time residuals r_i . In the classic least squares procedure, r_i is expressed as

$$r_i = t_i - t_0^{**} - T_i^{**}(h), \quad (4.1-16)$$

where r_i , the time residual caused by both measurement error and velocity uncertainties, is considered as a whole part. In the current procedure, this equation is changed to

$$r_i = t_i - t_0^{**} - (T_i(h^{**}, \langle m \rangle) + \Delta T_i(h^{**}, \langle m \rangle)), \quad (4.1-17)$$

where $\langle m \rangle$ is the mean value of different velocities. Since the velocities of the travel paths from the hypocenter to different stations are different from each other and the exact velocity values are never known, the following assumption is used: The actual velocity values are random variables, oscillating around the known mean velocity value. The mean value is thus taken as the true velocity. Thus in equation (4.1-17), $T_i(h^{**}, \langle m \rangle)$ stands for the exact travel time without error, $\Delta T_i(h^{**}, \langle m \rangle)$ is the travel time error resulted from velocity uncertainties, and t_i , the observed arrival time, contains the measurement error. The source parameter correction, $\delta\boldsymbol{\theta}$, is calculated using equation (4.1-14). In this method, Δt is still the time difference between observed t_i and calculated arrival time $t_0^{**} + T_i(h^*, m_i)$, where $T_i(h^*, m_i)$ is the travel time calculated using the actual velocity. The matrix \mathbf{A} is changed to

$$\mathbf{A} = \begin{bmatrix} 1 & \partial(T_1 + \Delta T_1)/\partial x_0 & \partial(T_1 + \Delta T_1)/\partial y_0 & \partial(T_1 + \Delta T_1)/\partial z_0 \\ \vdots & \vdots & \vdots & \vdots \\ 1 & \partial(T_n + \Delta T_n)/\partial x_0 & \partial(T_n + \Delta T_n)/\partial y_0 & \partial(T_n + \Delta T_n)/\partial z_0 \end{bmatrix}, \quad (4.1-18)$$

where ΔT_i is expressed as (Gibowicz and Kijko, 1994)

$$\Delta T_i = T_i(h^*, \langle m \rangle) \sigma_v^2 / \langle v_p \rangle^2 \quad (4.1-19)$$

where $\langle v_p \rangle$ is the mean value of the velocities, v_{pi} , σ_v is the standard deviation of v_{pi} , and the travel times are described by the formula $T_i(h^*, m) = d / v_{pi}$ (d is the source-receiver distance). The term \mathbf{C}_r in equation (4.1-14) is composed of two parts:

$$\mathbf{C}_r = \mathbf{C}_t + \mathbf{C}_T \quad (4.1-20)$$

Where \mathbf{C}_t is the diagonal matrix with variances of the arrival-time measurement errors σ_{ti}^2 , and \mathbf{C}_T is the diagonal matrix with diagonal elements equal to the travel-time variances σ_{Ti}^2 defined by the following expression (Gibowicz and Kijko, 1994)

$$\sigma_{Ti}^2 = (T_i(h, \langle m \rangle))^2 \sigma_v^2 / \langle v_p \rangle^2 \quad (4.1-21)$$

4.1.3. Relative Location Technique

In the classic least squares approach, the initial source parameters $\boldsymbol{\theta}^*$ may sometimes be poorly chosen and thus influences the final results. In the relative location procedure, a reference event R with known parameters $\boldsymbol{\theta}_R$, which is nearby the event to be located, is used. The time residuals are treated the same as in Fedorov's procedure. The arrival times of the reference event R is

$$t_{Ri} = t_{R0} + T(h_R, \langle m_{Ri} \rangle) + \Delta T(h_R, \langle m_{Ri} \rangle) + \varepsilon_{Ri} . \quad (4.1-22)$$

The location of the studied event is then obtained by adding correction parameters $\delta \boldsymbol{\theta}$ to the reference parameters $\boldsymbol{\theta}_R$, and no iteration is needed. The arrival time for R after

correction, including the measurement error is thus the observed arrival time at station i :

$$t_i = t_{R0} + \delta t_0 + T((h_R + \delta h), \langle m_{Ri} \rangle) + \Delta T((h_R + \delta h), \langle m_{Ri} \rangle) + \varepsilon_i \quad (4.1-23)$$

where ε_{Ri} in (4.1-22) and ε_i stand for the measurement error at station i for event R and for the event to be located, respectively. Applying the first order Taylor expansion to $T((h_R + \delta h), \langle m_{Ri} \rangle)$,

$$t_i = t_{R0} + \delta t_0 + T(h_R, \langle m_{Ri} \rangle) + \delta x_0 \partial T_i / \partial x_0 + \delta y_0 \partial T_i / \partial y_0 + \delta z_0 \partial T_i / \partial z_0 + \Delta T((h_R + \delta h), \langle m_{Ri} \rangle) + \varepsilon_i \quad (4.1-24)$$

Subtracting (4.1-22) from (4.1-24), if the reliability of arrival time measurements for both events is the same, ε_i and ε_{Ri} eliminate each other. Also assume the ray paths from the reference hypocenter R and the located hypocenter traverse the same structure, so the time anomalies $\Delta T(h_R, \langle m_{Ri} \rangle)$ and $\Delta T((h_R + \delta h), \langle m_{Ri} \rangle)$ caused by velocity uncertainties are approximately the same. Thus the following equation is obtained:

$$\delta t_i = t_i - t_{R0} = \delta t_0 + \delta x_0 \partial T_i / \partial x_0 + \delta y_0 \partial T_i / \partial y_0 + \delta z_0 \partial T_i / \partial z_0. \quad (4.1-25)$$

The matrix form of equation (4.1-25) is

$$\mathbf{A} \delta \boldsymbol{\theta} = \delta \mathbf{t}, \quad (4.1-26)$$

where \mathbf{A} is in the same form as defined in equation (4.1-11) except that its elements are calculated at the reference hypocenter R . $\delta \mathbf{t}$ is the time difference between the observed arrival times at both events. The corrected parameters $\delta \boldsymbol{\theta} + \boldsymbol{\theta}_R$ are the source parameters to be found.

4.1.4. Comparisons of Location Procedures

The relative location procedure is in general more accurate than the classical least squares procedure. It uses known reference event parameters instead of guessed initial source parameters, which may lead to a wrong solution due to the more than one minimum of the misfit function $\Phi(\theta)$. Also, the relative procedure is faster since it does not require iterations. In Fedorov's procedure, the error caused by velocity uncertainties is considered. This approach is possible if the fluctuations of velocity model parameters, from an average model, can be expressed in statistical terms. In practice, knowledge of the seismic velocities and their variances is usually adequate for this technique.

4.1.5. Location of Micro-Earthquakes in CHOP Wells

For the present case, since all the data available was recorded by only one receiver the exact source location is not able to be determined. With only one receiver, a small event close to the receiver cannot be distinguished from a larger one far from the receiver. But with the knowledge of the reservoir, a rough location of the source failure can still be estimated. It is known that the micro-seismicities are mostly caused by the cap rock failures occurring in the yielded zone surrounding the well bore. Since the distance between the wells in this case is about three or four hundred meters, the distance between the source failure and the receiver must be smaller than a few hundred meters. According to Samaroo (1999), the P-wave caused by the shale failure has a polarization orientation of approximately 20° from the horizontal plane. The formation thickness at the well 8B-36 is about 6 meters. Thus an estimate can be made that the source and receiver distance is around 16 meters. (Figure4-1)

4.2. Focal Mechanisms of Micro-Earthquakes in CHOP Wells

Micro-earthquakes occur in CHOP wells when the sand in the yielded zone cannot support the cap rock, shale, due to the removal of the sand matrix. This type of small seismic event is similar to mine tremors occurring in mines when the shaft in a mine is

removed. Because of this similarity, the mechanism of the micro-earthquakes in CHOP wells should be similar to that in mines. Since no systematic differences have been found between mine tremors and natural earthquakes so far, most of what has been discovered about the mechanism of earthquakes can be applied to mine tremors and then to CHOP wells.

Earthquakes occur as a result of the sudden release of energy within some confined regions undergoing deformation. As the region is deformed, energy is stored in the rocks in the form of elastic strain until the accumulated stress exceeds the strength of the rock. Then fracture or faulting occurs, and the opposite sides of the fault rebound to a position of equilibrium, and the energy is released in the form of heat, in the crushing of rock, and in the generation of seismic waves. If an earthquake is caused by faulting, then the direction of a fault should be related to the stresses acting within the Earth, which caused the fracture. And it is possible to estimate the direction of the fault along which an earthquake occurred from the record of seismic waves (Gibowicz and Kijko, 1994).

Focal mechanism studies of mine tremors confirmed that some of the events are caused by shear failures on fault planes in a rock mass. However, other mechanisms other than shear failure are possible. Inversion of the seismic moment tensor is the most general approach for determining a point source mechanism. Moment tensors describe completely in a first-order approximation the equivalent forces of general seismic point sources. Equivalent forces are defined as producing displacements at a given point that are identical to those from the real forces acting at the source. A seismic source is considered as a point when the spatial dimension of the source L is much smaller than the source-receiver distance r , and the time duration of the source L/c (where c is rupture velocity) is much smaller than the length of the observed seismic waves (Gibowicz and Kijko, 1994). Since the seismic source in the CHOP case is tiny, it can be regarded as a point source, and the mechanism of this source can be found by inversion of the seismic moment tensor.

4.2.1. Moment-Tensor Inversion

Since the external application of a force is unlikely to occur in natural earthquakes, it is more probable that the force action is of a self-balancing type, such as a pair of opposite forces acting simultaneously on two adjacent parts of the medium with the resultant force equal to zero (Gibowicz and Kijko, 1994). Such pair of forces of equal magnitude is called a force couple if they act along the positive and negative i direction, respectively, and at a small distance apart in j direction (the arm). The moment of this force couple is denoted as M_{ij} . In the rectangular coordinate system, there are three directions for the forces and the arm, so totally there are nine possible couples. The set of nine terms of M_{ij} , which is a second-rank tensor, is known as the moment tensor of the source and can be represented by a matrix \mathbf{M} with elements M_{ij} :

$$\mathbf{M} = \begin{bmatrix} M_{11} & M_{12} & M_{13} \\ M_{21} & M_{22} & M_{23} \\ M_{31} & M_{32} & M_{33} \end{bmatrix}. \quad (4.2-1)$$

If a general body force representing a seismic source can be expressed as a linear combination of force couples with different moments M_{ij} , then the displacement caused by this force is the sum of the displacements caused by each individual force couple.

Following Stump and Johnson (1977), the displacement u_k generated at a point x' at the time t' by a distribution of equivalent body-force densities f_i within a source volume V is given by

$$u_k(x', t') = \int_{-\infty}^{\infty} \int_V G_{ki}(x', t'; x, t) f_i(x, t) dx^3 dt \quad (4.2-2)$$

where G_{ki} is the Green's function containing the propagation effects between the source (x, t) and the receiver (x', t') . The origin of the coordinate system is placed at a convenient point within V and the Green's function is expanded in the series

$$G_{ki}(x', t'; x, t) = \sum_{n=0}^{\infty} \frac{1}{n!} x_{j_1} \cdots x_{j_n} G_{ki, j_1 \cdots j_n}(x', t'; 0, t). \quad (4.2-3)$$

The moment of the equivalent body force is defined as the force moment tensor

$$M_{ij_1 \cdots j_n}(0, t) = \int_V x_{j_1} \cdots x_{j_n} f_i(x, t) dx^3. \quad (4.2-4)$$

Substituting (4.2-3) and (4.2-4) to (4.2-2), the displacement becomes the convolution of the Green's function with the moment tensor

$$u_k(x', t') = \sum_{n=0}^{\infty} \frac{1}{n!} G_{ki, j_1 \cdots j_n}(x', t'; 0, 0) * M_{ij_1 \cdots j_n}(0, t'). \quad (4.2-5)$$

If the source dimensions are small in comparison to the observed wavelengths of seismic waves, only the first term in equation (4.2-5) needs to be considered. Also, the conservation of angular momentum for the equivalent body forces leads to the symmetry of the seismic moment tensor (Gilbert, 1970) so $M_{ij} = M_{ji}$ is a symmetric second-rank tensor. Then equation (4.2-5) becomes

$$u_k(x', t') = G_{ki, j}(x', t'; 0, 0) * M_{ij}(0, t') \quad (4.2-6)$$

where the moment tensor is time dependent. If all components of the moment tensor can be assumed to have the same time dependence $s(t)$, the displacement can be expressed as

$$u_k(x', t') = [G_{ki, j}(x', t'; 0, 0) * s(t')] M_{ij}. \quad (4.2-7)$$

And M_{ij} becomes a set of constants. Since the Green's functions represent the propagation effects and can be calculated by taking into account the geological structure between the source and the receiver, the location of the point source and the position of

the receiver, the moment tensor can be solved. If all components of the moment tensor cannot be assumed to have the same time dependence, this problem can be solved in the frequency domain. Equation (4.2-6) is then changed to the form

$$u_k(x', f) = G_{ki,j}(x', f; 0, 0) * M_{ij}(0, f). \quad (4.2-8)$$

Both equations (4.2-7) and (4.2-8) can be written in the matrix form

$$\mathbf{U} = \mathbf{G}\mathbf{M}. \quad (4.2-9)$$

When the moment tensor, which represents the source mechanism, is solved in the time domain, \mathbf{U} is the observed ground displacements of dimension n , which are recorded by a set of n receivers, \mathbf{G} is composed of the Green's functions for each receiver of dimension $n \times 6$, and \mathbf{M} is the moment tensor with elements $M_{11}, M_{12}, M_{13}, M_{22}, M_{23}, M_{33}$. The source time dependence function $s(t)$ can be found by some other means (Gibowicz and Kijlo, 1994). When the moment tensor is solved in the frequency domain, equation (4.2-8) is solved for each frequency.

When solving equation (4.2-9), singular value decomposition of \mathbf{G} is used and it can be expressed as

$$\mathbf{G} = \mathbf{W}\mathbf{Q}\mathbf{V}^T \quad (4.2-10)$$

where \mathbf{W} consists of the eigenvectors associated with the nonzero eigenvalues of $\mathbf{G}\mathbf{G}^T$, \mathbf{V} consists of similar eigenvectors for $\mathbf{G}^T\mathbf{G}$, and the diagonal members of \mathbf{Q} are the positive square roots of the nonzero eigenvalues of $\mathbf{G}^T\mathbf{G}$. The inverse of \mathbf{G} becomes

$$\mathbf{G}^{-1} = \mathbf{V}\mathbf{Q}^{-1}\mathbf{W}^T \quad (4.2-11)$$

and the moment tensor is solved by $\mathbf{M} = \mathbf{G}^{-1}\mathbf{U}$.

After the moment tensor is solved, the magnitude and direction of the principal stresses of the source can be determined from the eigenvalues and eigenvectors of the moment tensor. Since \mathbf{M} is a symmetric second-order tensor, its eigenvalues are all real and eigenvectors mutually orthogonal. It can be written in the form

$$\mathbf{M} = m_1 \mathbf{a}_1 \mathbf{a}_1 + m_2 \mathbf{a}_2 \mathbf{a}_2 + m_3 \mathbf{a}_3 \mathbf{a}_3 \quad (4.2-12)$$

where m_1, m_2, m_3 are eigenvalues of the symmetric second-order moment tensor, and $\mathbf{a}_1, \mathbf{a}_2, \mathbf{a}_3$ are the eigenvectors of the moment tensor. In the coordinate system $(\mathbf{a}_1, \mathbf{a}_2, \mathbf{a}_3)$, the stress vectors on coordinate planes are normal to the coordinate planes and the shearing stresses vanish on these planes. The directions $(\mathbf{a}_1, \mathbf{a}_2, \mathbf{a}_3)$ are the principal directions of stress and m_1, m_2, m_3 are the magnitudes of the principal stresses of the source.

In summary, the source mechanism of a micro-seismic event in the CHOP well can be found if the ground displacements from a set of receivers are available. The source moment tensor is calculated using the equation $\mathbf{U} = \mathbf{GM}$, and then the eigenvectors and eigenvalues of the moment tensor are taken as the directions and magnitudes of the principal stresses of the source.

4.3. Micro-Earthquake Magnitude

The strength of micro-earthquakes can be measured in terms of the seismic moment or of the earthquake magnitude. The seismic moment, also known as the scalar moment, is expressed as

$$M_0 = \mu \bar{u} A, \quad (4.3-1)$$

where μ is the shear modulus at the source, \bar{u} is the average displacement across the fault, and A is the fault area (Aki and Richards, 1980). It is a measure of the earthquake strength defined in terms of parameters of the double-couple shear dislocation source

model, and thus the most reliable and useful measure of the strength of a seismic event (Gibowicz and Kijko, 1994). However, to obtain the earthquake strength in an easier way, the magnitude is used.

4.3.1. Local Magnitude and Signal Duration Magnitude

The earthquake magnitude, which is a measure of the earthquake strength, quantifies the energy radiated over a fixed frequency band. The most popular used magnitude is the local magnitude M_L . It defines a standard size of earthquake and rates the others in a relative manner by their maximum amplitude under identical observational conditions.

$$M_L = \log A(\Delta) - \log A_0(\Delta), \quad (4.3-2)$$

where A is the maximum amplitude recorded on the Wood-Anderson seismogram for an earthquake at epicentral distance of Δkm , and A_0 is the maximum amplitude at Δkm for a standard earthquake. The standard earthquake, i.e. $M_L = 0$ in this formula, is such as to give the maximum trace amplitude of $1\mu m$ on a Wood-Anderson type seismograph at $\Delta = 100km$. Reduction of amplitudes observed at various distances to the expected amplitudes at the standard distance of $100km$ is made up by empirical functions obtained under the assumption that the ratio of the maximum amplitudes at two given distances is independent of the azimuth and is the same for all earthquakes.

Because the Wood-Anderson instruments have a limited dynamic range, it severely limited the magnitude range for which M_L can be estimated, and they seldom give useful records for earthquakes with magnitude less than 2. Figure4-2 and 4-3 show the ground displacements of a typical sharp P (shown in Figure3-8) and a diffuse P (Figure3-9) waves. Since the average thickness of the sand is only a few meters, and the depth of the formation is about five to six hundred meters, the size of the micro-earthquake sources could only be measured in centimeters. To estimate magnitude of micro-earthquakes recorded by high-gain instruments, other approaches are needed.

One approach is to calculate the ground motion from the recorded maximum amplitude, and from this compute the response expected from a Wood-Anderson seismograph. One possible method of this type of approach is to synthesizing the Wood-Anderson response by first deconvolving the seismogram with the response of the seismograph, and then convolving it with the response of the Wood-Anderson instrument.

In a general form, the local magnitude can be written as

$$M_A = \log A_{\max}^j + B \log R^j + C + D^j, \quad (4.3-3)$$

where M_A is the local magnitude of a given seismic event, A_{\max} is the maximum amplitude recorded at station j , B , C , and D^j are constants, and R is the source-receiver distance. The constants B , C , and D^j are found by applying the least squares regression method to a set of seismic events with known magnitudes (Gibowicz and Kijko, 1994).

Another approach to estimate the magnitude of micro-earthquake is known as the signal duration magnitude M_D ,

$$M_D = B \log \tau^j + C R^j + D + E^j, \quad (4.3-4)$$

where τ^j is the time at station j when the amplitude of the signal decays to the cutoff criteria specified for a given system. B , C , D and E^j are empirical constants. These constants are usually determined using the same method as that used to solve for the constants in (4.3-3).

4.4. Seismic Energy

The radiated seismic energy represents the total wave energy radiated by an earthquake. It is also used as a measure of the strength of seismic events. The energy radiated in a body wave (P or S) was derived by Boatwright and Fletcher (1984) and expressed as follows:

$$E_s^P = 4 \pi \langle F^P \rangle^2 (R^P / F^P)^2 \varepsilon_P^* \quad (4.4-1)$$

$$E_s^S = 4 \pi \langle F^S \rangle^2 (R^S / F^{Si})^2 \varepsilon_{Si}^* \quad (4.4-2)$$

These equations relate the total energy radiated in the body wave (E_s^P or E_s^S) to the energy flux (ε_P or ε_{Si}) contained in the P - or S - wave arrival. The energy flux ε contained in a body wave is the product of the density, the wave velocity, and the integral of the square of the particle velocity:

$$\varepsilon(\mathbf{x}) = \rho c \int_0^\tau \dot{u}^2(\mathbf{x}, t) dt \quad (4.4-3)$$

where \dot{u} is the ground velocity at receiver \mathbf{x} and time t , c is the body wave velocity and τ is the body wave duration. The asterisk in (4.4-1) and (4.4-2) indicates that the measurement of the energy flux has been corrected for the body-wave attenuation. To correct for the attenuation, the energy loss is assumed to be the simple frequency dependence

$$A(\omega) = e^{-\omega T / Q} \quad (4.4-4)$$

where T is the travel time and Q the quality factor. The corrected energy flux in the frequency domain is thus

$$\varepsilon^*(\mathbf{x}) = \frac{\rho c}{\pi} \int_0^\infty |\dot{u}^2(\mathbf{x}, \omega)|^2 e^{+\omega T / Q} d\omega. \quad (4.4-5)$$

F^P and F^S are the radiation pattern coefficients. R^P and R^S are the geometrical spreading factors, which are simply expressed as the source-receiver distance R . The subscripts and superscripts i for the S -waves indicate that the energy flux measurement

and the radiation pattern correction are specific to a single component of motion (SV or SH components). $\langle F^P \rangle^2 = 4/15$ and $\langle F^S \rangle^2 = 2/5$ are the mean square radiation pattern coefficients (Boatwright and Choy, 1986). The equation

$$E_S = 4\pi \langle F \rangle^2 \frac{\sum \varepsilon_c^*(x_n) R^2(x_n)}{\sum (F^c)^2} \quad (4.4-6)$$

where the summation index running over the measurements of $\varepsilon_c(x_n)$ at the station locations, x_n , estimates the energy radiated in P - or S - wave from the measurements of the energy flux in a set of arrivals (Boatwright and Fletcher, 1984). When the effects of directivity are taken into account, equations (4.4-1) and (4.4-2) can be modified to

$$E_S^P = 4\pi \langle F^P \rangle^2 \frac{\langle \psi_\alpha \rangle}{\psi_\alpha} \left(\frac{R^P}{F^P} \right)^2 \varepsilon_P^* \quad (4.4-7)$$

$$E_S^S = 4\pi \langle F^S \rangle^2 \frac{\langle \psi_\beta \rangle}{\psi_\beta} \left(\frac{R^S}{F^{Si}} \right)^2 \varepsilon_{Si}^* \quad (4.4-8)$$

where function ψ_c describes the directivity of the wave type c . When the angle between the direction of a seismic ray leaving the source and the direction of rupture propagation is small, the recorded ground motion may be considerably increased in amplitude.

The total seismic energy for small seismic events is $E = E_P + E_S$. In the present case, the seismic energy is the energy of the P -wave, since there is only P -wave propagating in the sand.

4.5. Direction of Polarization

In the CHOP well, the observed body wave is of a single type – the P -wave. An S -wave is unlikely since in the yielded zone, sand exists only in a suspended form and it

cannot support the shear stress. For a compressional wave, the particle displacements are in the direction of the wave propagation. If the direction of particle displacements (polarization orientation) is known from the observed three-component data, the wave propagation direction can be obtained.

The calculation of the polarization direction can be performed as follows (Kanasewich, 1981). Given three-component ground displacement data, a time window ΔT is selected over each of the three orthogonal components of ground motion. Over this time window, a covariance matrix is calculated for all three components (R -radial, T -tangential and Z -vertical). Then the eigenvector corresponding to the largest eigenvalue is regarded as the polarization direction. Assume there are N points within the time window ΔT , so $\Delta T = N\Delta t$ where Δt is the sample rate. The covariance matrix is expressed as

$$V = \begin{bmatrix} \text{cov}[Z, Z] & \text{cov}[Z, T] & \text{cov}[Z, R] \\ \text{cov}[T, Z] & \text{cov}[T, T] & \text{cov}[T, R] \\ \text{cov}[R, Z] & \text{cov}[R, T] & \text{cov}[R, R] \end{bmatrix} \quad (4.5-1)$$

where $\text{cov}[R, T]$ is computed as

$$\text{cov}[R, T] = \frac{1}{N} \sum_{i=1}^N (x_{Ri} - \mu_R)(x_{Ti} - \mu_T) \quad (4.5-2)$$

where μ is the mean value of the ground displacement, x , over N observations:

$$\mu = \frac{1}{N} \sum_{i=1}^N x_i. \quad (4.5-3)$$

However the results of the calculation are strongly affected by noise contamination and the chosen of the time window. Applying this method to the diffuse P -wave shown in Figure3-9 over the time interval 0.031~0.033s, the calculated eigenvalues are

$$D = \begin{bmatrix} 0.0001 & 0 & 0 \\ 0 & 0.0074 & 0 \\ 0 & 0 & 0.1391 \end{bmatrix} \times 10^{-13} \quad (4.5-4)$$

with the largest eigenvalue 0.1391×10^{-13} . The eigenvector corresponding to it is $E = [-0.3328 \ 0.1383 \ 0.9328]$ and the angle between this eigenvector and the horizontal direction is 19.4° , which is comparable to the 20° angle described by Samaroo. While applying to Figure3-8, the sharp P -wave, over the same time interval, the derived angle is 60° . This may be explained that in the yielded zone, a near-wellbore area is more homogeneous than the area that is farther away from the wellbore. Of course noise is included in this calculation and these angles may not be very accurate, but they should be close to the true values due to the knowledge we have about the yielded zone.

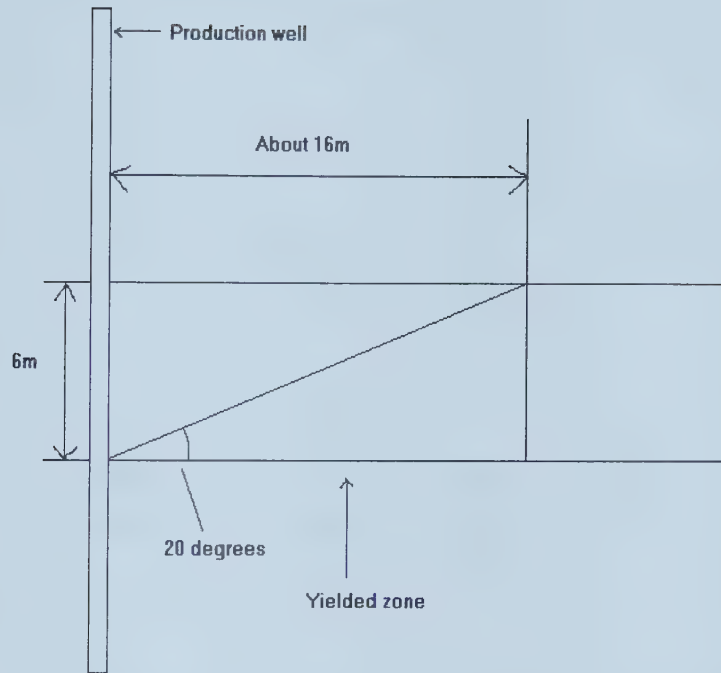


Figure4-1 Estimated micro-seismic source-receiver distance.

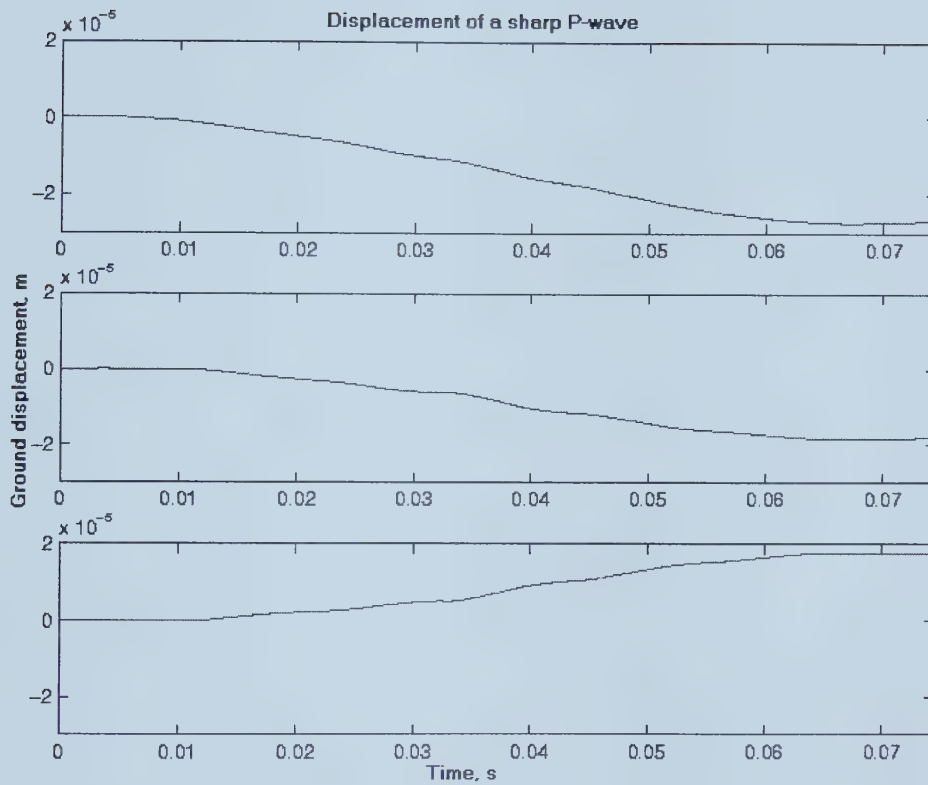


Figure4-2 Displacement of a typical sharp P-wave. The three panels from top to bottom are the vertical, radial and tangential components, respectively.

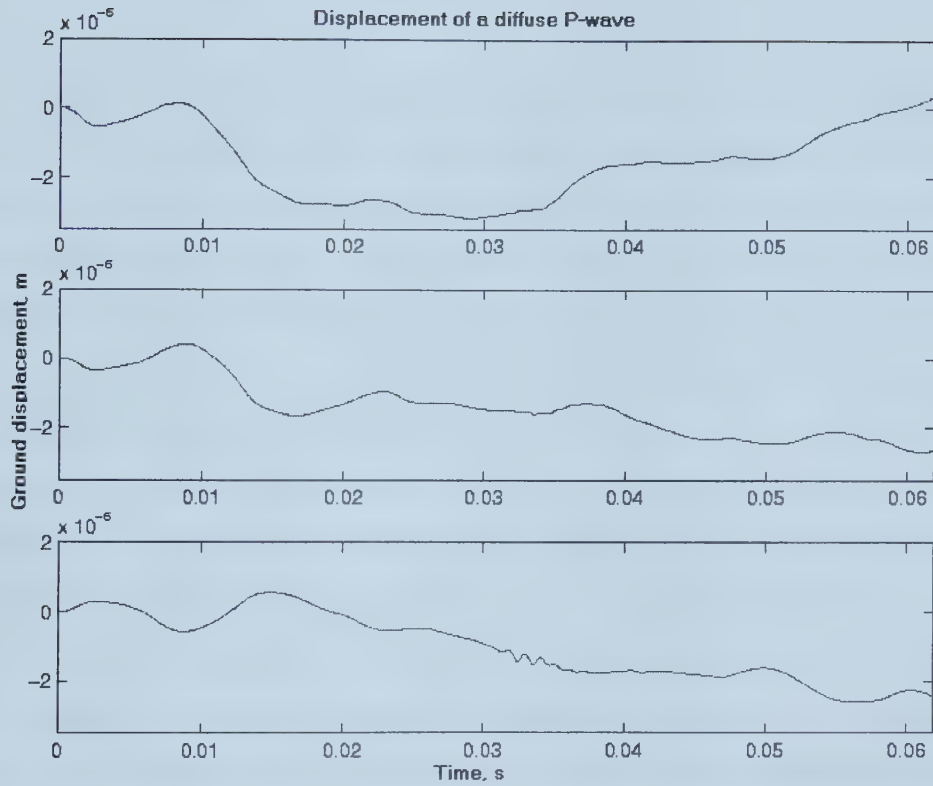


Figure4-3 Displacement of a typical diffuse P-wave. The three panels from top to bottom are the vertical, radial and tangential components, respectively.

5. Two Phase Miscible Flow – the Dispersion Phenomenon in Porous Media

5.1. The Phenomenon of Dispersion

In a miscible displacement experiment, when one fluid is introduced into the porous medium filled with another fluid, a sharp front between fluid phases is produced. As the introduced fluid displaces the fluid originally filled in the porous medium, the front may deform resulting in viscous fingering or broaden as a result of dispersion. In the transition zone the displacing and displaced fluid mix together, and this transition zone increases with time both longitudinally (in the direction of the average flow), and transversally (normal to the direction of average flow).

Dispersion usually happens due to two factors: mechanical dispersion and molecular diffusion. A common interpretation by engineers and geologists is that mechanical dispersion is usually the dominant mechanism in longitudinal dispersion and molecular diffusion usually assumed to count for transverse dispersion (Bear and Bachmat, 1990).

The factors that cause mechanical dispersion are flow and the presence of a pore system. That is, the velocity variations in the pore system cause this phenomenon. At the pore scale, a zero velocity is usually assumed at the solid surface, and a maximum velocity at some internal point of every pore cross section (Figure5-1a). This maximum velocity varies due to the shape of the pore space. It is the shape of the pore space that causes the fluctuation of the microscopic streamlines with respect to the direction of the average flow (Figure5-1b). This fluctuation causes any initially close cloud of component particles to spread, and these particles will occupy an ever-growing volume of the flow domain as flow continues. So it is the pore size distribution and the shape of the pore spaces that causes velocity variations, and velocity variations cause mechanical dispersion. However, the dispersion caused by velocity variations is primarily in the flow direction, i.e. longitudinal dispersion; velocity variations alone cannot explain the particle spreading in the direction normal to the average flow direction, i.e. transverse dispersion.

Molecular diffusion happens by the random motion of the molecules when a concentration difference exists. The component particles tend to move from the higher concentration region to the lower concentration region. This phenomenon occurs whenever the fluid is at rest or the fluid flows, and it happens in two directions. The velocity variations produce a concentration gradient in the direction of average flow, so the particles tend to move toward the low concentration region longitudinally. However, this effect is small compared to the longitudinal dispersion caused directly by velocity variations. At the same time, particles tend to move laterally, because a concentration gradient is also produced across the streamlines. It is this phenomenon that accounts for transverse dispersion (Figure5-1c).

5.2. The Convection-Diffusion Theory

The equations usually used for describing dispersion (Fried and Combarnous, 1971) are given by:

$$\frac{\partial(c_i)}{\partial t} + \nabla \cdot (c_i \mathbf{v}) = \nabla \cdot (\rho \mathbf{D} \cdot \nabla (\frac{c_i}{\rho})), \quad i = 1 \cdots 2, \quad (5.2-1)$$

where c_i , $i = 1 \cdots 2$, are the mass concentrations of each fluid, ρ is the total fluid density, \mathbf{v} is the velocity of the fluid, and \mathbf{D} is the dispersion tensor accounting for both mechanical dispersion and diffusion. The summation of this equation over all fluids produces the continuity equation:

$$\frac{\partial \rho}{\partial t} + \nabla \cdot (\rho \mathbf{v}) = 0 \quad (5.2-2)$$

The fractional concentration, c_{fi} , defined by

$$c_{fi} = \frac{c_i}{\rho}, \quad (5.2-3)$$

permits (5.2-2) to be written as

$$\frac{dc_{fi}}{dt} = \frac{\partial c_{fi}}{\partial t} + \mathbf{v} \cdot \nabla c_{fi} = \frac{1}{\rho} \nabla \cdot (\rho \mathbf{D} \cdot \nabla(c_{fi})), \quad i = 1 \cdots 2. \quad (5.2-4)$$

In the limiting case where molecular diffusion becomes zero we may refer to the volume fraction of space occupied by a fluid phase, i.e. $1 = S_1 + S_2$, where $S_i = V_i / V$.

Here

$$S_1 = \frac{\rho_2(1 - c_{f2})}{\rho_2 + (\rho_1 - \rho_2)c_{f2}} \quad (5.2-5)$$

and

$$c_{f2} = \frac{\rho_2(1 - S_1)}{\rho_2 + (\rho_1 - \rho_2)S_1} \quad (5.2-6)$$

To simplify this case, the total density is assumed to be constant, then (5.2-2) and (5.2-4) become

$$\nabla \cdot \mathbf{v} = 0 \quad (5.2-7)$$

and

$$\frac{dc_{fi}}{dt} = \frac{\partial c_{fi}}{\partial t} + \mathbf{v} \cdot \nabla c_{fi} = \nabla \cdot (\mathbf{D} \cdot \nabla(c_{fi})), \quad i = 1 \cdots 2, \quad (5.2-8)$$

respectively. The velocity is usually taken to be the average fluid velocity $\mathbf{v} = \mathbf{u}$. This is called the Dupuit-Forchheimer assumption.

If we take the fluid velocity along the x -axis only, and separate the dispersion tensor into longitudinal and transverse components to the velocity, (5.2-8) becomes

$$\frac{\partial(c_{f2})}{\partial t} + v \frac{\partial(c_{f2})}{\partial x} = D_L \frac{\partial^2 c_{f2}}{\partial x^2} + D_T \left(\frac{\partial^2 c_{f2}}{\partial y^2} + \frac{\partial^2 c_{f2}}{\partial z^2} \right). \quad (5.2-9)$$

In a strictly one-dimension flow, we would set the transverse term on the right-hand of this equation to zero to obtain

$$\frac{\partial(c_{f2})}{\partial t} + v \frac{\partial(c_{f2})}{\partial x} = D_L \frac{\partial^2 c_{f2}}{\partial x^2}. \quad (5.2-10)$$

The effluent concentration, which is defined as the ratio of the mass of displacing fluid emitted per unit time to the total mass emitted per unit time:

$$c_e = \frac{c_2 \mathbf{v}_2 \cdot \mathbf{n} A}{\rho \mathbf{v} \cdot \mathbf{n} A}, \quad (5.2-11)$$

becomes

$$c_e = c_{f2} - \frac{D_L}{v} \frac{\partial(c_{f2})}{\partial x}, \quad (5.2-12)$$

where \mathbf{n} is the surface normal of the emitting surface A , and \mathbf{v}_2 is the velocity of fluid2.

A solution to equation (5.2-12) under the ‘flowing concentration’ boundary conditions

$$v = u = \text{Constant}, \quad (5.2-13)$$

$$c_e = 0, \quad t \leq 0, \quad x \geq x_0, \quad (5.2-14)$$

$$c_e = 1, t > t_0, x = x_0, \quad (5.2-15)$$

$$c_e = 0, t > t_0, x = \infty, \quad (5.2-16)$$

is given by

$$c_e(x, t) = P\left(\frac{u(t - t_0) - (x - x_0)}{\sqrt{2D_L(t - t_0)}}\right) \quad (5.2-17)$$

in terms of the normal distribution $P(x)$ (Bear, 1988; Stalkup, 1982; Fried and Combarnous, 1971). An alternative form of this equation is

$$x = x_0 + u(t - t_0) - P^{-1}(c_e)\sqrt{2D_L(t - t_0)}. \quad (5.2-18)$$

The normal distribution $P(x)$ has the property that

$$P(-1) \cong 0.16, P(1) \cong 0.84, \quad (5.2-19)$$

which makes it convenient to use the concentration values 0.84 and 0.16 to specify the width of the front. We get

$$w(t) = x(c_{e0.16}, t) - x(c_{e0.84}, t) = 2\sqrt{2D_L(t - t_0)}. \quad (5.2-20)$$

The rate of front broadening is therefore

$$\frac{dw(t)}{dt} = \frac{\sqrt{2D_L}}{\sqrt{(t - t_0)}} \quad (5.2-21)$$

and the acceleration of the broadening is

$$\frac{d^2 w(t)}{dt^2} = -\frac{\sqrt{D_L}}{2(t-t_0)^{3/2}}. \quad (5.2-22)$$

Hence, we see that the convection-diffusion theory predicts that the width of dispersion front increases in time but that the widening decelerates.

5.3. The Dynamical Equations of Two-Phase Flow

In the limiting case of zero surface tension and negligible molecular diffusion the equations of immiscible fluid flow and miscible fluid flow yield equivalent flow description. This limiting case supplies a useful check on the self-consistency of the two flow descriptions and the dynamics of dispersion. In this section the equation of immiscible fluid flow will be considered.

Here we assume two phase flow in porous media and neglect the effects of inertia and viscous dissipation within the fluids. Under these conditions the equations of motion are given by (in one dimension) (Udey and Spanos, 1993)

$$Q_{11}q_1 - Q_{12}q_2 = -\frac{\partial P_1}{\partial x}, \quad (5.3-1)$$

$$Q_{22}q_2 - Q_{21}q_1 = -\frac{\partial P_2}{\partial x}, \quad (5.3-2)$$

$$P_1 - P_2 = \beta \frac{\partial S_1}{\partial t}. \quad (5.3-3)$$

where q_i is the volumetric flow rate of fluid i .

Here three equations are required to completely specify Newton's second law since we have three degrees of freedom in strain rate. These variables are the volumetric flow

rates of the two phases and the rate of change of the relative proportions of the two phases. These equations are supplemented by the continuity equation

$$\frac{\partial S_1}{\partial t} + \frac{1}{\eta} \frac{\partial q_1}{\partial x} = 0. \quad (5.3-4)$$

Together these four equations may be used to determine the four unknowns $q_1, q_2, P_1 - P_2$ and S_1 . Assuming that the total volumetric flow rate $q = q_1 + q_2$ is constant (the Buckley-Leverett assumption), these equations may be reduced to three equations

$$\frac{\partial(P_1 - P_2)}{\partial x} = -(Q_{11} + Q_{12} + Q_{22} + Q_{21})q_1 + (Q_{12} + Q_{22})q \quad (5.3-5)$$

$$P_1 - P_2 = \beta \frac{\partial S_1}{\partial t} \quad (5.3-6)$$

$$\frac{\partial S_1}{\partial t} + \frac{q}{\eta} \frac{\partial f_1}{\partial x} = 0 \quad (5.3-7)$$

where $f_1 = \frac{q_1}{q}$. In order to follow along a given saturation contour we require $\frac{dS_1}{dt} = 0$.

i.e. $\frac{\partial S_1}{\partial t} + v_s \frac{\partial S_1}{\partial x} = 0$, where v_s is the velocity of the saturation contour. A given saturation contour may be described by the saturation as a function of position and time $S_1(x, t)$. It may also be described by specifying the saturation at a specific time and finding out where in space it is $x(S_1, t)$. Here

$$\frac{\partial}{\partial t} x(S_1, t) = v_s(S_1, t). \quad (5.3-8)$$

Now consider two saturation values S_L and S_H (low and high) where $S_H > S_L$. The distance between these two saturations is given by

$$w(S_L, S_H, t) = x(S_H, t) - x(S_L, t). \quad (5.3-9)$$

Here

$$\frac{\partial}{\partial t} w(S_L, S_H, t) = v_s(S_H, t) - v_s(S_L, t), \quad (5.3-10)$$

$$\frac{\partial^2}{\partial t^2} w(S_L, S_H, t) \begin{cases} < 0 \text{ dispersion decelerates (front narrowing)} \\ = 0 \text{ dispersion is constant} \\ > 0 \text{ dispersion accelerates (front broadening)} \end{cases} \quad (5.3-11)$$

When this theory is reformulated in the context of miscible fluid flow Udey and Spanos (1993) have demonstrated that the convection-diffusion equation is not obtained. Their analysis yielded a Fokker Plank equation plus the additional dynamic pressure equation given in equation (5.3-3). It has been demonstrated in this section that this additional degree of freedom yields constant and accelerating dispersion effects not allowed for by the convection-diffusion equation.

5.4. Experimental Results

The conditions under which dispersional instabilities occur have many similarities to the conditions for viscous fingering (Cyr et al., 1988). Thus the relative importance of the two instabilities must be considered in cases where large viscosity contrasts exist. A first order stability analysis of each instability allows one to determine the dominant instability process (Cyr et al., 1988; Udey and Spanos, 1993). In the present case of equal viscosities the frontal motion is dominated by heterogeneities and dispersion.

The following figures show the experiment setup and the results obtained from a two-phase flow experiment by using dyed water to displace clean water. The determination of the constant saturation contour was obtained by eye, so human error exists besides the error caused by the measuring tool which is shown as error bars on the graphs. The graphs obtained under 0.5m head show that the dispersion front increases at a nearly constant rate. This may be explained that it is due to the very close viscosity of the two phases and the homogenous packing of the porous medium. With 0.75m head, the dispersion front increases at a slightly decelerating rate.

The observation can be explained as follows:

Dispersion is enhanced by a large pore size distribution, which has been demonstrated by Yang (1997). Dispersion is also enhanced by the adverse mobility ratio (viscosity divided by permeability). Adverse mobility ratio indicates that the displacing fluid is less viscous than the displaced phase. Favorable mobility ratio indicates that the displacing fluid is more viscous than the displaced phase. Favorable mobility ratio suppresses dispersion. These results are demonstrated by Cyr et al. (1988).

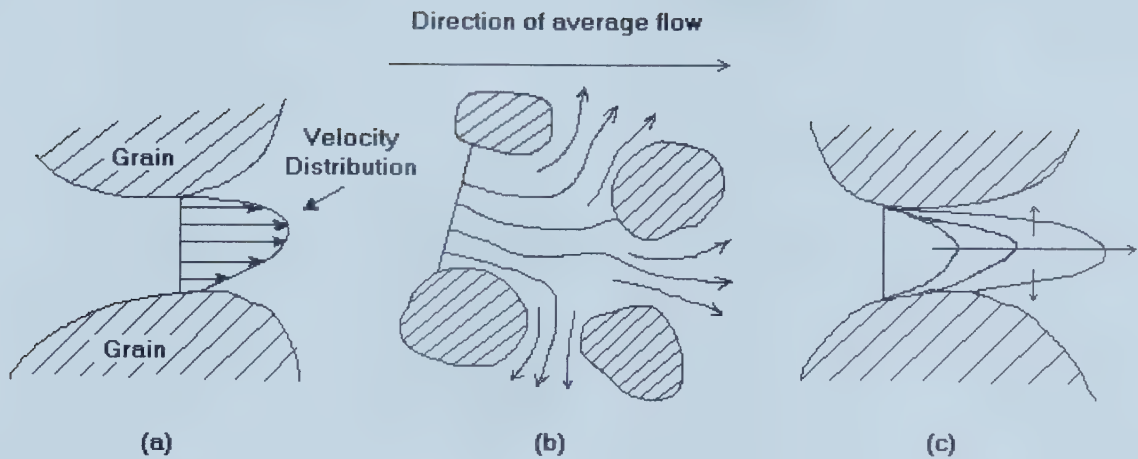


Figure5-1 Spreading due to mechanical spreading (a), (b), and molecular diffusion (c) (bear and Bachmat, 1990). The velocity is zero at the grain surface and maximum somewhere between the grains (a). The size of the pore between the grains causes the different maximum velocities and thus the fluctuation of the streamlines (b). Particles move from the high concentration area to low concentration area (c).

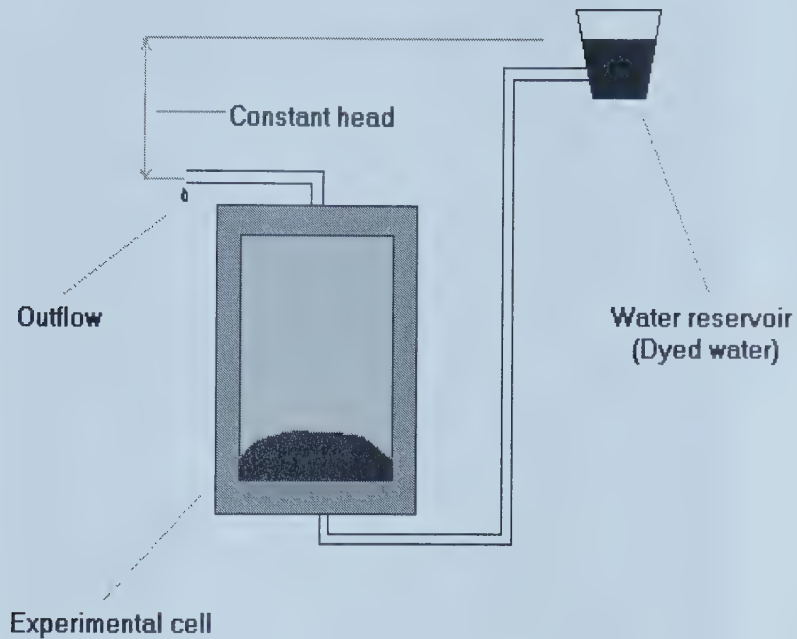


Figure5-2 A diagram showing the dispersion experiment setup. The experimental cell was filled with sand and clean water originally and the dyed water displaced the clean water during the experiment. The water reservoir was filled with dyed water and its level was kept constant.

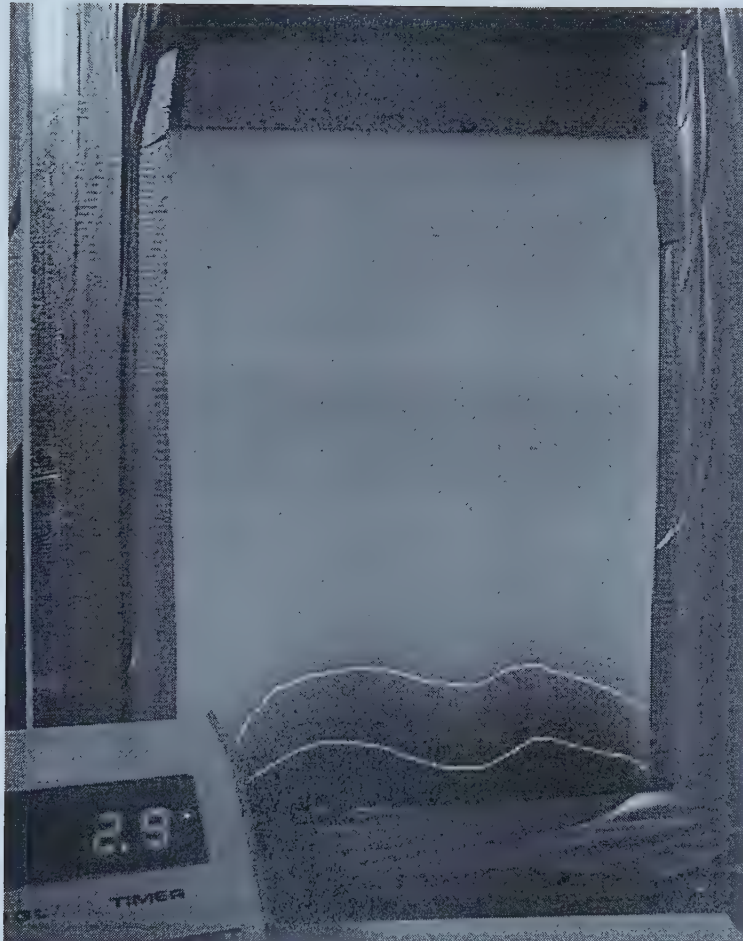


Figure5-3 A picture showing the dispersion front at time 2.9s. The dark area at the bottom with two lines on it is the displacing fluid – the dyed water. These two lines are the two constant-saturation lines being measured.

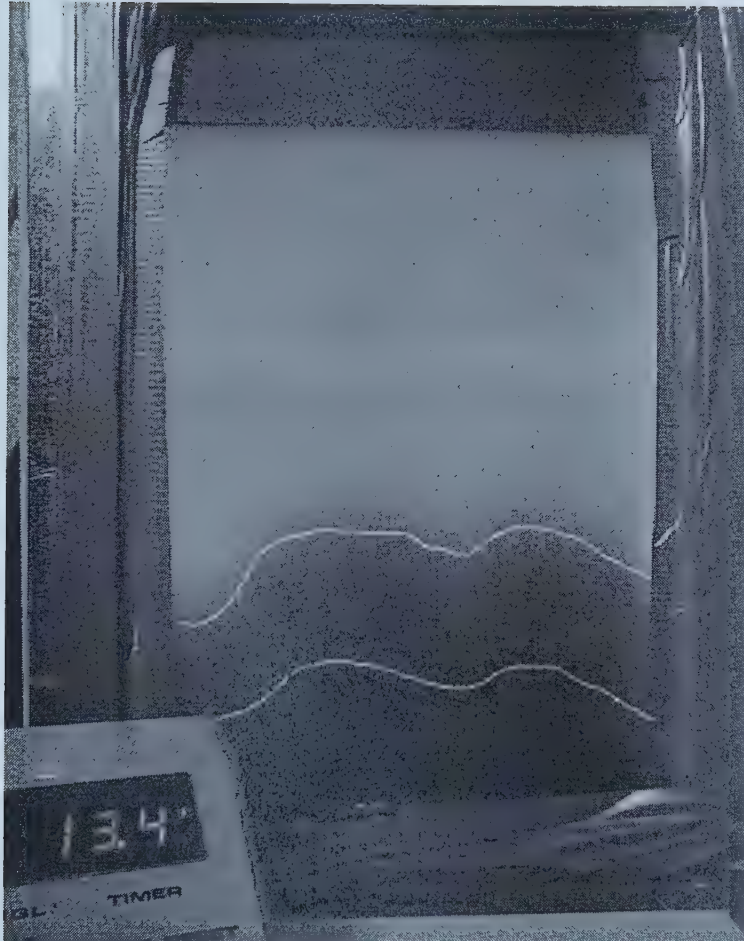


Figure5-4 A picture showing the dispersion front at time 13.4s. The dark area at the bottom with two lines on it is the displacing fluid – the dyed water. These lines are the same constant-saturation lines being measured as in Figure5-3.

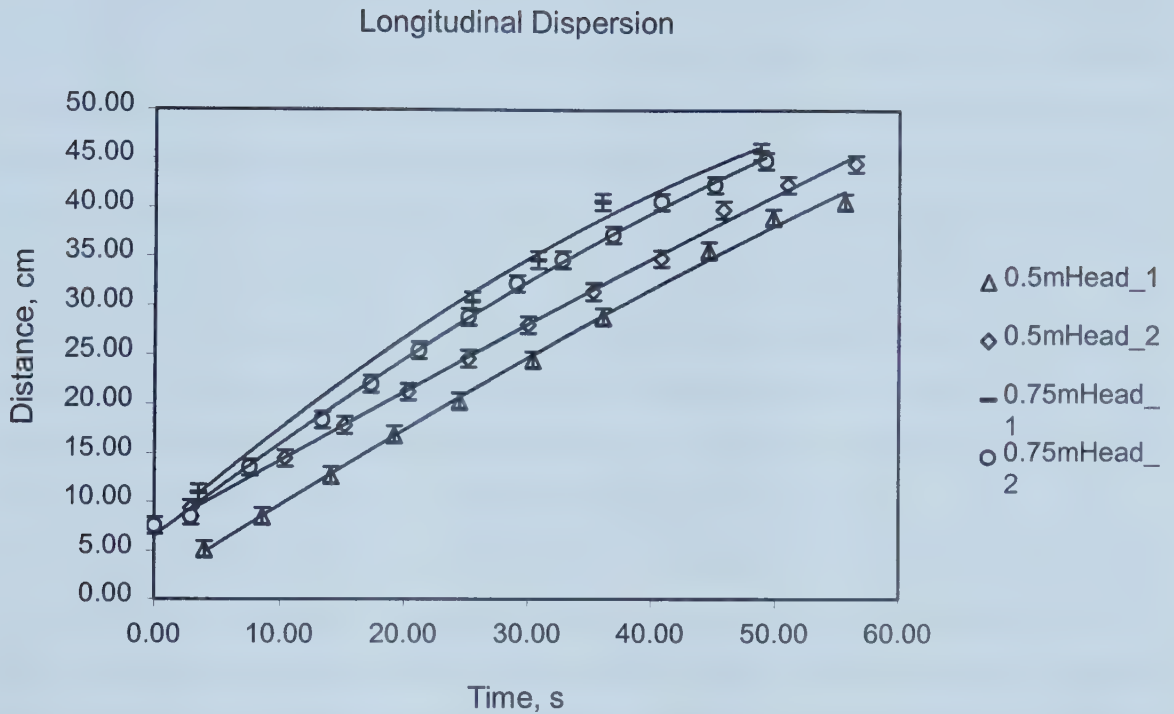


Figure5-5 Longitudinal dispersion at four different cases. These data were obtained by measuring the distance between the two constant-saturation contours showing in figures 5-3 and 5-4 at different times. The experiments of 0.5mHead_1 and 0.5mHead_2 had the same constant pressure but started at different times. So did the experiments of 0.75mHead_1 and 0.75mHead_2.

6. Discussion

In this project, micro-seismic techniques were used in CHOP wells to monitor the production process. Data collected with an accelerometer placed in the wellbore indicates that micro-seismic monitoring is able to monitor the sand production and detect the abnormal operation of the production tools. Examination of the micro-seismic data shows that the micro-seismic signatures of a PC pump changes significantly during periods of abnormal operation. Periods of high sand content within the fluid being transported by the pump were not only detected, but could also be predicted, based on the detection of large triggered events which are considered to be stick-slip failure at the intact reservoir/sand crumbling zone. Prediction of excess sand influx is a useful tool, since procedures can be taken to prevent the damage of the PC pump.

The micro-seismic events caused by the shale failure are estimated to be located around 16 meters from the wellbore, according to the polarization orientation of the P-wave. The source mechanism of the events may be found if data from more receivers are available. It is a useful method to decompose the source moment tensor to find the source type and the principal stresses of the source. The size of the micro-earthquakes is too small to be measured in the local magnitude scale associated with the Wood-Anderson instruments. The ground displacement of a typical wave in this case is only a few micrometers. It is possible to measure the size of the micro-earthquakes using generalized local or signal duration magnitude, provided that ground displacements from several receivers are available. The total seismic energy in the present case is only the energy of the P-wave, since there is no S-wave in this case due to the suspension form of the sand. It can be found when the source-receiver distance and the directivity of the source are both known. From the P-wave polarization calculation, the source is found to be inside the yielded zone with about 20° for a typical diffuse P-wave and 60° for a sharp one. Error may be included in the calculation due to noise.

For future work in micro-seismic monitoring of cold heavy oil production, more receivers and more reliable receivers should be used so that more accurate source parameters including the source location, magnitude, seismic energy and the source mechanism could be found.

In Chapter 5, two theories describing the dispersion phenomenon are presented. In the convection-diffusion theory, the pressure difference between phases is believed to be zero, since there is no surface tension. It predicts that the width of the dispersion front increases in time but the widening decelerates. However, physical consistency requires an equation $P_1 - P_2 = \beta \frac{\partial S_1}{\partial t}$ in order to specify the pressure drop in the direction of flow. Also Udey and Spanos (1993) have shown that the convection diffusion equation must be replaced by a Fokker Plank equation to obtain consistency between pore scale and macroscale descriptions. This theory allows for the width of the dispersion front to increase at a constant rate or accelerate. In the laboratory experiments, if the displacing fluid is more viscous than the displaced fluid, the dispersion usually decelerates, and if the displacing fluid is less viscous than the displaced fluid, the dispersion usually accelerates. The experimental results are obtained by visually examining the isosaturation contour, which include human errors. For future experiments, a quantitative method may be used to define the isosaturation contour.

References

1. Aki, K. and Richards, P. G. (1980). Quantitative Seismology. Theory and Methods. W. H. Freeman, San Francisco.
2. Bear, J. (1988). Dynamics of Fluids in Porous Media, Dover, New York.
3. Bear, J. and Bachmat, Y. (1990). Introduction to Modelling of Transport Phenomena in Porous Media, Kluwer Academic Publishers, Boston.
4. Bear, J. and Buchlin, J-M. (1991). Modelling and Applications of Transport Phenomena in Porous Media, Kluwer Academic Publishers, Boston.
5. Boatwright, J. and Choy, G. L. (1986). Teleseismic Estimates of the Energy Radiated by Shallow Earthquakes. Journal of Geophysical Research 91, 2095-2112.
6. Boatwright, J. and Fletcher, J. B. (1984). The partition of radiated energy between *P* and *S* waves. Bulletin of the Seismological Society of America 74, 361-376.
7. Chugh, S., Baker, R. and Telesford, A. (2000). Mainstream Options for Heavy Oil: Part I – Cold Production. Journal of Canadian Petroleum Technology 39, 31-39.
8. Cyr, T. J., De La Cruz, V. and Spanos, T. J. T. (1988). An Analysis of the Viability of Polymer Flooding as an Enhanced Oil Recovery Technology. Transport in Porous Media 3, 591-618.
9. Davidson, B., Spanos, T. J. T. and Dusseault, M. (1999). Laboratory Experiments on Pressure Pulse Flow Enhancement in Porous Media. Presented and Published in the Proceedings of the CIM Regina Technical Meeting, Oct. 1999.
10. Dunning, N. E., Henley, G. J. and Lange, A. G. (1980). The Freemont Field, An Exploration Model for the Lloydminster Area, SaskOil Publication, August 1980.
11. Dusseault, M. B., Geilikman, M. and Spanos, T. J. T. (1998). Mechanisms of Massive Sand Production in Heavy Oil Reservoirs, A Paper Presented at the

- 1998 UNITAR Conference on Heavy Oils and Tar Sands, Beijing, PRC, 26-30 Oct., 1998.
12. Fried, J. J. and Combarnous, M. A. (1971). Dispersion in Porous Media. *Adv. Hydrosci.* 7, 169-282.
 13. Gibowicz, S. J. and Kijko, A. (1994). *An Introduction to Mining Seismology*, Academic Press, San Diego.
 14. Gilbert, F. (1970). Excitation of the Normal Modes of the Earth by Earthquake Sources. *Geophys. J. Roy. Astr. Soc.* 22, 223-226.
 15. Hardy, H. R., Jr. (1977). *Proceedings/First Conference on Acoustic Emission/Microseismic Activity In Geologic Structures And Materials*. Trans Tech Publications, Clausthal, Germany.
 16. Hyne, N. J. (1991). *Dictionary of petroleum exploration, drilling & production*, Tulsa, Okla.: PennWell Pub. Co.
 17. Jupe, A., Cowles, J. and Jones, R. (1998). Microseismic Monitoring: Listen and See the Reservoir. *World Oil* 219, 171-174.
 18. Kanasewich, E. R. (1981). *Time Sequence Analysis in Geophysics*, University of Alberta Press, Edmonton.
 19. Lee, W. H. K. and Stewart, S. W. (1981). *Principles and Applications of Microearthquake Networks*, Academic Press, New York.
 20. Lienert, B. R., Berg, E. and Frazer, L. N. (1986). Hypocenter: An Earthquake Location Method Using Centered, Scaled, and Adaptively Damped Least Squares. *Bulletin of the Seismological Society of America* 76, 771-783.
 21. McCallum, G. T. (1981). *Geology Needed for Heavy Oil*, McCallum, Stewart and Associates.
 22. Nyland, E. and Dusseault, M. B. D. (1983). Fireflood Micro-seismic Monitoring: Results and Potential for Process Control, *Journal of Canadian Petroleum Technology* 22, 62-66.
 23. Samaroo, M. (1999). *Pressure Pulse Enhancement: Report on the First Reservoir Scale Experiment*. A Project Submitted to the University of Waterloo in Fulfillment of the Project Requirement for the Degree of Master of Science in Earth Sciences.

24. Stalkup, F. I. Jr. (1982). Miscible Displacement, Monograph 8, Henry L. Doherty Memorial Fund of AIME, and Society of Petroleum Engineers of AIME, New York.
25. Stump, B. W. and Johnson, H. R. (1977). The Determination of Source Properties by the Linear Inversion of Seismograms. Bulletin of the Seismological Society of America 67, 1489-1502.
26. Udey, N. and Spanos, T. J. T. (1993). The Equations of Miscible Flow with Negligible Molecular Diffusion. Transport in Porous Media 10, 1-41.
27. Yang, D. (1997). A Thermodynamic Automaton and Some Applications. PhD Thesis, University of Alberta.

University of Alberta Library



0 1620 1423 3520

B45617